



저작자표시-비영리-변경금지 2.0 대한민국

이용자는 아래의 조건을 따르는 경우에 한하여 자유롭게

- 이 저작물을 복제, 배포, 전송, 전시, 공연 및 방송할 수 있습니다.

다음과 같은 조건을 따라야 합니다:



저작자표시. 귀하는 원저작자를 표시하여야 합니다.



비영리. 귀하는 이 저작물을 영리 목적으로 이용할 수 없습니다.



변경금지. 귀하는 이 저작물을 개작, 변형 또는 가공할 수 없습니다.

- 귀하는, 이 저작물의 재이용이나 배포의 경우, 이 저작물에 적용된 이용허락조건을 명확하게 나타내어야 합니다.
- 저작권자로부터 별도의 허가를 받으면 이러한 조건들은 적용되지 않습니다.

저작권법에 따른 이용자의 권리는 위의 내용에 의하여 영향을 받지 않습니다.

이것은 [이용허락규약\(Legal Code\)](#)을 이해하기 쉽게 요약한 것입니다.

[Disclaimer](#)

공학박사학위논문

이식형 보철기구를 위한 섬유 기반의
자력 이송 플렉서블 약물 전달 시스템

Fiber-based Pumpless Flexible Drug Delivery
System for Implantable Prosthesis

2014 년 8 월

서울대학교 대학원

기계항공공학부

변재환

이식형 보철기구를 위한 섬유 기반의 자력 이송 플렉서블 약물 전달 시스템

Fiber-based Pumpless Flexible Drug Delivery System
for Implantable Prosthesis

지도교수 전 누리

이 논문을 공학박사 학위논문으로 제출함

2014년 4월

서울대학교 대학원

기계항공공학부

변재환

변재환의 공학박사 학위논문을 인준함

2014년 5월

위원장 : _____

부위원장 : _____

위원 : _____

위원 : _____

위원 : _____

Abstract

Fiber-based Pumpless Flexible Drug Delivery System for Implantable Prosthesis

Jaehwan Byun

School of Mechanical and Aerospace Engineering

The Graduate School

Seoul National University

This thesis describes the design, fabrication and characterization of a novel, flexible, LCP-based implantable probe with integrated fiber-embedded drug drug-delivery channel. The novel design integrates fibers to fabricate monolithic probe with electrical components to achieve local drug delivery with minimum increase in implantable prosthesis thickness. The fabrication process for integrated drug delivery channel is described. Electrical performance and fluid delivery via characteristic of fluidic channel was also thoroughly tested. The key characteristic of the system is simple fabrication process that involves monolithic thermal bonding of fibers between flexible probes instead of complicated patterning and etching steps. Kevlar fibers were sandwiched between two LCP (liquid crystal polymer) film-based MEA (multiple electrode array probes) probes to serve as drug delivery channel. A custom thermal press mold was developed to bond electrode patterned LCP films and

fiber-containing films without damaging fragile MEA (micro electrode array) and interconnections during fabrication. We have measured the cyclic voltammetry, impedance spectroscopy of the integrated probe which has 64 electrodes, and the result shows a good compatibility of fabrication process. The embedded Kevlar-fiber channel provides self-driven fluid transport via the gap around the fiber bundle and capillary wicking via the interfilament space, respectively. The flow rate via the single fiber channel was characterized using 1% agarose gel as a brain phantom and the flow rate was 10^{-2} ~ 10^{-1} $\mu\text{l}/\text{min}$. Drug delivery to brain can be modeled as an absorptivity competitive system. The mathematical modeling of diffusion behavior in brain phantom has been established, and the model was correlated and verified with experimental results successfully. The flow rate via fiber-embedded channel is a function of concentration and molecular weight of the drug, the absorptivity of target tissue and the geometrical factor of the fiber. Finally, drug reservoir module compatible with fiber inlet has been developed and introduced. To solve a tight fitting joint with fiber, selective capillary flow technique using hydrophobic barrier was developed. This thesis has potential for application in a number of implantable medical devices.

Keywords: Pumpless, Capillary flow, Drug delivery, Porous fiber, Kevlar, Liquid Crystal Polymer (LCP) film, Flexibility, Implantable neural probes.

Student Number: 2008-30857

Contents

Abstract	i
Contents	iii
List of Tables	v
List of Figures	vii
Nomenclature	xii
Chapter 1 Introduction	1
11.1 A history of drug delivery channel for a neural prosthesis	1
1.2 Motivation and objectives	4
1.3 Thesis overview and contribution	6
Chapter 2 Pumpless flexible drug delivery channel		9
2.1 Concept	9
2.2 Materials	12
2.2.1 Liquid Crystal Polymer	12
2.2.2 Aramid family Kevlar fiber	13
2.2.3 LCP film-based Micro Electrode Arrays	15
2.3 Integration of fiber-embedded channel and MEA	18
2.3.1 Design	18
2.3.2 Asymmetric thermal pressure lamination process		21
2.3.3 Electrical features of the integrated device	29

2.3.4	Results and discussion	32
Chapter 3	Study of drug delivery performance	34
3.1	The capillary kinetics in Kevlar fibers	34
3.1.1	The capillary kinetics of pre-wetted and dry Kevlar fiber	34
3.1.2	The capillary kinetics of various geometric variation of fiber	37
3.2	Drug diffusion dynamics in agarose gel	41
3.2.1	Physical and mathematical modeling	43
3.2.2	Experimental data	46
3.2.3	Computational Estimation of diffusing behavior	61
3.2.4	Result and discussion	69
3.3	Drug delivery via the fiber-embedded channel	72
3.3.1	Measurement of flow rates	73
3.3.2	Functionality	77
Chapter 4	Drug reservoir module	82
4.1	Sealing mechanism	84
4.2	Design and assembling	86
4.4	Limitations and future works	88
Chapter 5	Conclusions	90
	Bibliography	96
	Abstract in Korean	105

List of Tables

Table 2.1	Measurement of steady state temperature with cooling condition	25
Table 2.2	Measurement of steady state temperature without cooling condition	26
Table 2.3	Integration results according to SV of temperature and pressure condition	28
Table 3.1	Regression coefficients l_{FC} and R value of the penetration length against t (min)	48
Table 3.2	Regression functions α_x and R value of sample no.1 without tension and twisting	49
Table 3.3	Regression functions α_x and R value of sample no.2 without tension and twisting	50
Table 3.4	Regression functions α_x and R value of sample no.3 without tension and twisting	51
Table 3.5	Regression functions α_x and R value of sample no.1 with 3N tension and without twisting	52
Table 3.6	Regression functions α_x and R value of sample no.2 with 3N tension and without twisting	53
Table 3.7	Regression functions α_x and R value of sample no.3 with 3N tension and without twisting	54
Table 3.8	Regression functions α_x and R value of sample no.1 without tension and with twisting of 520/m	55
Table 3.9	Regression functions α_x and R value of sample no.2 without tension and with twisting of 520/m	56
Table 3.10	Regression functions α_x and R value of sample no.3 with 3N tension and twisting of 520/m	57

Table 3.11	Regression functions α_x and R value of sample no.1 with 3N tension and twisting of 520/m	58
Table 3.12	Regression functions α_x and R value of sample no.2 with 3N tension and twisting of 520/m	59
Table 3.13	Regression functions α_x and R value of sample no.3 with 3N tension and twisting of 520/m	60
Table 3.14	Regression coefficient $\alpha_{0,FC}$, ξ_{FC} and l_{FC}	63
Table 5.1	Comparison list of fiber-embedded drug delivery channel system and conventional system	91

List of Figures

Figure 1.1	Various type of the flexible neural probes with microfluidic channel by micromachining. A. Metz <i>et al.</i> , 2004 B. Dominik Ziegler <i>et al.</i> , 2006 C. Jonathan T.W.Kuo <i>et. al.</i> , 2013 D. Chunyan Li <i>et al.</i> , 2009	2
Figure 2.1	Schematic of diagram and photographs of the flexible neural probe with fiber-embedded drug delivery channel	10
Figure 2.2	Microscope images of Kevlar fiber. A. 40X image of filaments. B. 20X image of the cross-section of red dye filled fiber	14
Figure 2.3	Lamination scheme of LCP film-based Micro Electrode Arrays	16
Figure 2.4	Photograph of recording/stimulus electrode of 64 ch. LCP film-based MEA	17
Figure 2.5	Photograph of connector side of 64 ch. LCP film-based MEA	17
Figure 2.6	Aluminum mold compatible with 64 ch. MEA. A. Male mold and partial enlarged images. B. Female mold	19
Figure 2.7	Photograph of all components for the flexible neural probe with fiber-embedded drug delivery channel	19
Figure 2.8	Parts lamination sequence for the integration process	21
Figure 2.9	Photograph of the asymmetric thermal pressure lamination process and temperature ramping profile	23
Figure 2.10	3D rendering image of mold assembly	24
Figure 2.11	Estimation of steady state temperature inside mold with cooling	25

Figure 2.12	Estimation of steady state temperature inside mold without cooling	26
Figure 2.13	Illustration of the assembled mold and components	27
Figure 2.14	Comparison of wiring state on recording/stimulation site before and after integration process	29
Figure 2.15	Impedance spectroscopy of the 64 ch. electrodes after integration process	31
Figure 2.16	Measured cyclic voltammetry of Au electrode site in phosphate buffered saline (PBS) at 50 mV/s	31
Figure 2.17	Examples of defective devices due to over- heating and/or over pressure	33
Figure 3.1	The capillary kinetics of pre-wetted and dry Kevlar fiber	36
Figure 3.2	The capillary kinetics of various conditions of fiber	37
Figure 3.3	Coaxial porosity and capillary inhibition length according to various conditions of fiber	40
Figure 3.4	Illustration and photograph of experiment setup	42
Figure 3.5	Physical modeling of the diffusion behavior in agarose gel	43
Figure 3.6	An example of a filtered image using the max entropy thresholding method	47
Figure 3.7	The kinetics of capillary front against time	48

Figure 3.8	Plot of the diffusion radius R against t and x . Sample no.1 without tension and twisting	49
Figure 3.9	Plot of the diffusion radius R against t and x . Sample no.2 without tension and twisting	50
Figure 3.10	Plot of the diffusion radius R against t and x . Sample no.3 without tension and twisting	51
Figure 3.11	Plot of the diffusion radius R against t and x . Sample no.1 with 3N tension and without twisting	52
Figure 3.12	Plot of the diffusion radius R against t and x . Sample no.2 with 3N tension and without twisting	53
Figure 3.13	Plot of the diffusion radius R against t and x . Sample no.3 with 3N tension and without twisting	54
Figure 3.14	Plot of the diffusion radius R against t and x . Sample no.1 without tension and with twisting of 520/m	55
Figure 3.15	Plot of the diffusion radius R against t and x . Sample no.2 without tension and with twisting of 520/m	56
Figure 3.16	Plot of the diffusion radius R against t and x . Sample no.3 without tension and with twisting of 520/m	57
Figure 3.17	Plot of the diffusion radius R against t and x . Sample no.1 with 3N tension and twisting of 520/m	58
Figure 3.18	Plot of the diffusion radius R against t and x . Sample no.2 with 3N tension and twisting of 520/m	59
Figure 3.19	Plot of the diffusion radius R against t and x . Sample no.3 with 3N tension and twisting of 520/m	60
Figure 3.20	Regression plot of coefficient $\alpha_{0,FC}$ and ξ_{FC} against geometrical variation of fiber	63

Figure 3.21	Comparison of experimental diffusion behavior in agarose gel and numerical estimation profiles in 10,20,30 min, respectively. No tension and twisting	65
Figure 3.22	Comparison of experimental diffusion behavior in agarose gel and numerical estimation profiles in 10,20,30 min, respectively. 3N tension and no twisting	66
Figure 3.23	Comparison of experimental diffusion behavior in agarose gel and numerical estimation profiles in 10,20,30 min, respectively. No tension and twisting of 520/m	67
Figure 3.24	Comparison of experimental diffusion behavior in agarose gel and numerical estimation profiles in 10,20,30 min, respectively. 3N tension and twisting of 520/m	68
Figure 3.25	Capillary inhibition length C toward opposite side of agarose gel and absorbed length A according to geometric variation of fiber	70
Figure 3.26	Plot of $R_{x=L(0)}(t)/L(t)$ ratio of diffusion profile against time t (min) according to geometric variation of fiber ..	71
Figure 3.27	Illustration of the experimental setup and the comparison graph of flow rate according to dye and molar concentration. 1X aCSF is control	74
Figure 3.28	The comparison graph of the flow rate according to twisting number of embedded-fiber	75
Figure 3.29	Time-lapse images of sequential drug delivery via fiber-embedded channel	77
Figure 3.30	Time-lapse images in case of drug delivery toward a contact surface of two 2% agarose gel blocks	79
Figure 3.31	Three different stages of drug delivery process	80
Figure 4.1	Illustration of sealing idea using a hydrophobic barrier ..	84
Figure 4.2	Time-lapse images of capillary flow in Kevlar fiber penetrated PDMS barrier	85

Figure 4.3	Rendering image of the drug reservoir module compatible with the 64 ch. integrated device	86
Figure 4.4	The prototype of drug reservoir module. A. Photographs of parts. B. Assembled image	87
Figure 4.5	Time-lapse images of capillary flow in Kevlar fiber penetrated PDMS coated drug chamber	88
Figure 4.6	Photograph of final assembled system including 64 ch ...	89
Figure 5.1	Rendering image of the flexible LCP film-based neural probe with the fiber-embedded drug delivery channels ...	92

Nomenclature

T_m	Melting temperature
P	Coaxial porosity
R	Diameter of fiber bundle
r	Diameter of single filament
N	Number of filaments
R_E	Capillary flow resistance
τ	Split ratio
t_n	N^{th} time step
$L(t_n)$	Length of capillary front at time t_n
$\bar{L}(t)$	Matrix of $L(t_n)$
$R_n(x, t)$	Radius of spherical diffusion in gel
$\bar{r}(t)$	Matrix of $R_n(x, t)$
$\bar{R}(t)$	Augmented matrix of $\bar{L}(t)$ and $\bar{r}(t)$
$\alpha_n(x)$	A coefficient of lateral diffusion at t_n and $L(t_n)$
ξ	A longitudinal attenuation factor of α
l_{FC}	Regression coefficient of $L(t_n)$
H	Heaviside function

Chapter I

Introduction

1.1 A history of drug delivery channel for a neural prosthesis

Implantable probes are widely used in academic and clinical applications to investigate the functions of brain network and to treat diseases such as Parkinson's disease and deafness, respectively. Neural prosthesis devices are typical active therapy instruments that are used to regenerate neuronal activity by electrical stimulation of the neural system. Implantable neural prosthesis devices are mainly classified based on their materials, i.e., silicon, metal, and polymer, and each type of device has its own advantages and disadvantages[1]. Recently, several groups have developed silicon-based electrode arrays for implantable probes using MEMS techniques. The stiff property of Si combined with their sharp profiles, they often cause inflammation around the implanted site [2-4]. As an alternative, flexible prosthetic devices using materials such as parylene [5, 6], polyimide [7-12] and liquid-crystal polymers (LCP) have recently been reported. Lee *et al.* reported general monolithic encapsulation platforms for various neural prosthetic devices based on LCP,

which has a very low degree of water absorption (<0.04%) and has good biocompatibility [13-17]. In addition to neural implantable devices, LCP-based neural prosthesis has the potential to be applied widely in cochlear implant devices[18], deep-brain stimulation devices [19] for Parkinson's disease, and in artificial retinal implant devices as visual prostheses[17]. Because it can be fabricated as a flexible film thinner than 50 μm , LCP film-based neural prosthesis offers the advantage of matching the mechanical rigidity of the recording site with surrounding tissue.

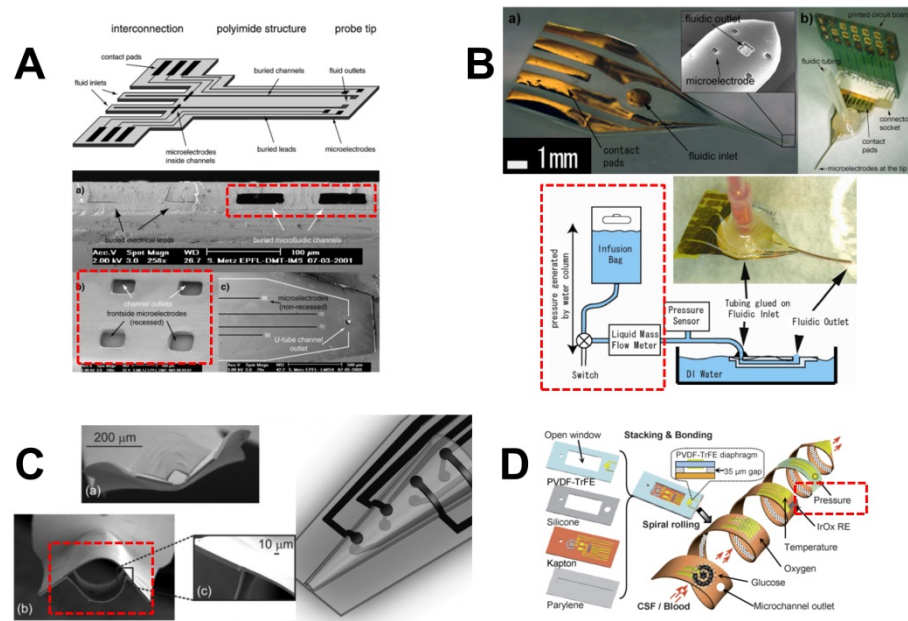


Figure 1.1 Various type of the flexible neural probes with microfluidic channel by micromachining. **A.** Metz *et al.*, 2004 **B.** Dominik Ziegler *et al.*, 2006 **C.** Jonathan T.W.Kuo *et al.*, 2013 **D.** Chunyan Li *et al.*, 2009

In chronically implanted devices, foreign body reaction such as inflammation and scar formation at the implant site is an important issue

because tissue reaction can lead to implant rejection and deteriorate the stability of electrical signal acquisition and delivery [20-27]. Novel fabrication approaches to incorporate microfluidic channels on implantable probes have been reported. Some groups have realized drug delivery with surface coatings containing soluble factors such as polyethylene glycol (PEG) [28, 29] and polyethyleneimine (PEI) [30]. A nano-porous coated electrode used to adjust the electrical impedance has been developed to improve the signal-to-noise ratio (SNR) of a chronic implantable system [23, 31, 32]. Other groups have developed a drug-eluting electrode that contains drugs within a biodegradable polymer matrix [25, 27, 33-35]. Although these types of channel have several advantages, there is a critical limitation of continuous drug delivery because coated materials and a biodegradable matrix are irreversible and disposable. For the long-term implantation, continuous time of drug release and controllability of flow rate must be essential functions.

On the other hand, microfluidic channel systems based on conventional etching techniques have been reported. Metz *et al.* have reported an embedded multi-channel microfluidic drug delivery channel using batch-fabricated combining polyimide micromachining and a lamination technique [8]. Takeuchi *et al.* have presented various types of microfluidic channel on parylene layer by sacrificial layer method and thermal bonding of layers [6, 9, 36]. Recently, J.T.W. Kuo *et al.* demonstrated 3D sheath structural parylene C based neural probe [5]. In terms of micro-scale, fluidic channels by etching and deposition techniques definitely are advantageous to reduce a feature dimension of system, whereas auxiliary pumps are needed to transfer liquid

stream via microchannel. By the result, whole system including signal process parts and pumps becomes more complex.

Due to difficulty of integrating etched channels with LCP material during thermal bonding step, drug delivery channels have not been reported until now. Early attempts to fabricate channels by lamination of groove-shaped preformed LCP films failed due to clogged or collapsed channels during thermal laminating step. In addition, the design was structurally susceptible to blocking caused by mechanical deformation such as bending or folding during implantation.

1.2 Motivation and objective

In the near future, we will encounter a super-aged society that has an elderly population of more than 20 percent. As increasing an elderly population, nervous system diseases would be an important issue because most of nervous system diseases are related to a quality of life. For examples, representative diseases of central nerve system, there are Parkinson's disease, depressive disorder and epilepsy. In addition, peripheral nerve system diseases such as trigeminal neuralgia, Bell's palsy, carpal tunnel syndrome and hearing impairment are even common in wide range of age. Nervous system diseases do not directly lead patients to death, while high socioeconomic cost is caused.

More researches are interested in the field of neural prosthesis and they have developed various types of devices and tried to occupy fundamental and original technologies for drug delivery micro-channels. As mentioned above, conventional technologies until now are mainly based on a micromachining technology with high cost and low productivity, so it is not yet available commercially.

The first aim of this thesis is to develop a commercially available technology for a drug delivery channel system. For this purpose, several design factors have been introduced;

- (1) Pumpless drug delivery system
- (2) Low cost and mass productivity based on simplified fabrication process
- (3) Applicability with LCP film-based micro electrode array (MEA)
- (4) Compatibility of deep brain stimulus system (DBS)
- (5) Biocompatibility and stability of long-term implantation
- (6) Flexibility

First, the study of a pumpless system among these factors is a prominent and fundamental development objective, and the overall dimension of the whole system including auxiliary parts (pump, digital signal processing module, drug and electrical power source, etc.) can be minimized than conventional systems. Second, our approach should be compatible with LCP film-based neural probes. LCP film-based

MEA have many advantages as an application of neural probe. Therefore, the drug delivery systems for this probe have to preserve the inherent characteristics of LCP. Finally, novel fabrication techniques are needed to reduce cost and to enable a mass productivity for commercialization. Finally, this thesis is aiming to realize a whole system including a functional drug reservoir module.

1.3 Thesis overview and contribution

This paper describes the development of Kevlar fiber-embedded drug-delivery channel for implantable microprobe applications. This is the first report of functional drug delivery channel for LCP-based flexible probes. We describe a thermal laminating approach that use a low temperature melting LCP layer as a guide layer that also function as an adhesive layer.

In chapter 2, the properties of LCP and Kevlar fiber we used are introduced and the fabrication process of LCP film-based MEA is explained at first. Next, the integration process and the results of parametric study of integration condition are reported. The inside steady state temperature of thermal pressure mold for was estimated by boundary element method. In the end of chapter 2, electrical features of the integrated device are presented. We found that electric circuit of the integrated device works normally; electrical properties of the integrated probe were measured with success without breaking and/or shortage of wiring.

In chapter 3, the characteristics of the fiber-embedded drug delivery channel are demonstrated. For a controllability of flow rate in fiber and fiber embedded channel, the kinetics of capillary flow in Kevlar fiber was studied and the flow rate in the integrated probe was characterized using 1% agarose gel as a surrogate of brain. In addition, a diffusion behavior of ‘absorption- absorption competitive system’ is modeled. Furthermore the physical modeling and the numerical estimation of diffusion behavior were established, and the numerical result was verified by experimental data. As the results in chapter 2, we found that the geometric variations of fiber are a core factor determining the flow rate of drug in fiber channel.

In chapter 4, the prototype of drug reservoir is presented. We developed a novel non-sealing connecting method which is compatible with fiber-embedded channel. Especially, the non-sealing connecting method we developed would be a fundamental technology for the type of fiber-embedded drug delivery system.

Generally, nervous system diseases are chronic and difficult to recovery completely by medicine treatments. Neural prosthesis is promising medical applications for patients with central and/or peripheral nervous system diseases. Many research groups have gradually studied and developed elaborate neural prosthesis. Recently, they have tried to combine a neural prosthesis with a drug delivery channel. Reliable drug delivery channel is one of the important functions because this channel is essential for long-term implantation and an efficacy of electrical treatment.

Due to a complexity of fabrication and manufacturing, most of previous researches are not available to commercialize. In addition, hollow microfluidic

channels for drug delivery have to be connected with portable pumps to infuse drugs, and also this type of channel is mechanically vulnerable to physical deformation and damage.

The main contribution of this research is to provide a novel and innovative drug delivery system which has a potential for applications in a number of implantable medical devices including neural prosthesis.

Chapter II

Pumpless flexible drug delivery channel using capillary flow in fiber

2.1 Concept

The main physical concept of this research is based on capillary action via fiber threads. Capillary flow in fiber is a common phenomenon in everyday life, for example wiping a face with a towel. In the textile industry, capillary flow in textile media has been extensively investigated because it is directly related to dyeing and coating efficiency of either fabrics or yarns.

One of the objectives in this research is to realize a pumpless drug delivery system which enables continuous flow of drug. Capillary flow in a porous structure is the only method to deliver continuous liquid stream without external force. Porous structure as a pipeline can be fabricated in micro-scale using expendable polymer matrix mixed with solvents. However, it is necessary to form a longitudinal homogeneity of geometric variation such as porosity, cross-sectional perimeter of void, etc. Therefore synthetic fibers, representative porous structure, might be an excellent alternative because single filament of synthetic fiber shows extremely fine

surface roughness and low rugosity. Consequently, a synthetic fiber gives a homogeneous geometrical factor; hence we can engineer and manipulate the flow characteristics of drug delivery via fiber bundles.

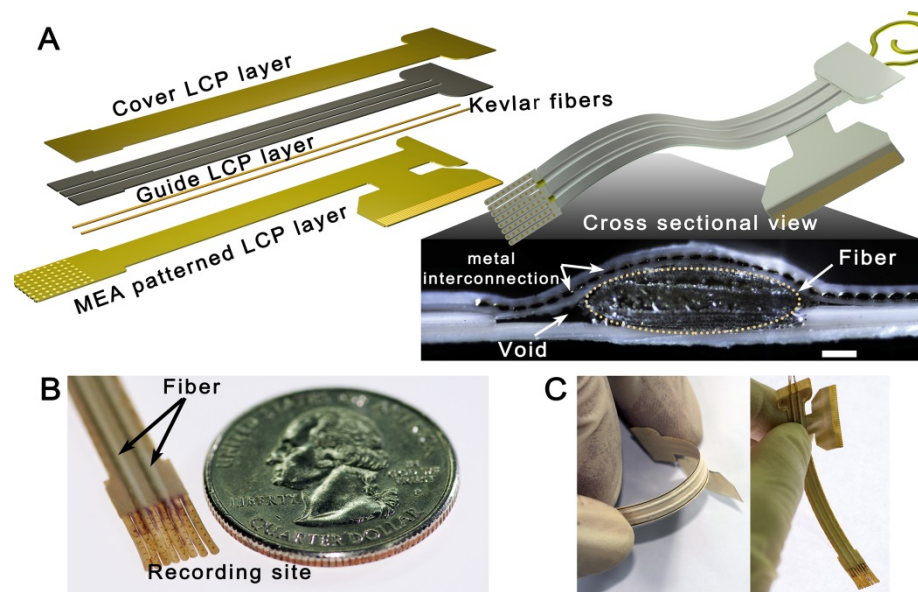


Figure 2.1 Schematic of diagram and photographs of the flexible neural probe with fiber-embedded drug delivery channel

Schematic diagram and photographs of the flexible neural probe with pumpless drug delivery channel is shown in Figure 2.1 . The total thickness of the probe including the fiber-embedded drug channels is 300 μ m. The probe is assembled by aligning three LCP film layers to form monolithic sealed device with 64 ch. electrode. Two drug delivery channels were placed along the length of the

implant. The cross-section given in figure 2.1 shows a distinct void region around the elliptically formed Kevlar fiber. The originally round fiber (dia. 600 μ m) shows slightly distorted elliptical geometry (680 x 190 μ m) after the pressure/thermal bonding step. The distorted shape does not influence the function of the drug delivery channel as the fiber and void region can be used for passive and active fluid delivery, respectively. This void region can be applied as an extrude channel for pressure driven flow.

Stimulation/recording sites shown in figure 2.1 B were patterned on 8 comb-like strips with the drug delivery ports located close to them. The comb-like structure was designed to enhance contact with the tissue as well as diffusion of anti-inflammatory drug around the opposite side of the electrodes. The photographs given in figure 2.1 C indicate the flexibility of the integrated device.

2.2 Materials

2.2.1 Liquid Crystal Polymer

Liquid crystal polymer (LCP) is a flexible thermoplastic polymer with unique electrical and physical property that is widely used in electronic packaging applications as a substrate for high density printed circuit and wiring board[37]. LCP has very low water absorption coefficient (below 0.04% by weight) and shows excellent biocompatibility. Due to excellent mechanical, electrical and biocompatible properties, LCP has been used for bioMEMS applications [14, 15, 17, 37, 38], including as a substrate for planar neural probes.

LCP films were obtained in thin film form. Since LCP does not react with most chemicals, LCP films should be bonded each other by thermal pressure lamination. The melting temperature of commercial LCP films ranges over 280°C, however, LCP films can be bonded below the melting point by applying slight pressure[37].

Two types of LCP films were used in this work; 1) low temperature ($T_m=280^\circ\text{C}$) used for metallization substrate and guide layer that also serves the function of bonding layer and 2) high temperature LCP ($T_m=315^\circ\text{C}$) used for cover layer and window layer. LCP can be directly laminated to another LCP layer without using an adhesive layer as it softens to a flowable state and hardens

when cooled. Therefore, it is critical to precisely control bonding temperature to selectively melt and flow the guide LCP layer without damaging fragile thin film metal interconnects and electrodes. It is also important to keep the temperature on the metalized LCP substrate to below melting temperature by cooling the mold assembly from the top while metalized substrate is placed facing the cooled heat sink side of the mold

2.2.2 Aramid family Kevlar fiber

As briefly described earlier, to sandwich fibers between LCP films require a thermal lamination step at temperatures as high as 280°C. Natural fibers such as cotton and silk cannot be used with LCP-film based probes due to low resistance to high temperatures. Synthetic fibers such as polyethylene, polyester, and polypropylene exhibit good biocompatibility but they also have low melting temperatures, significantly below LCP thermal bonding temperature.

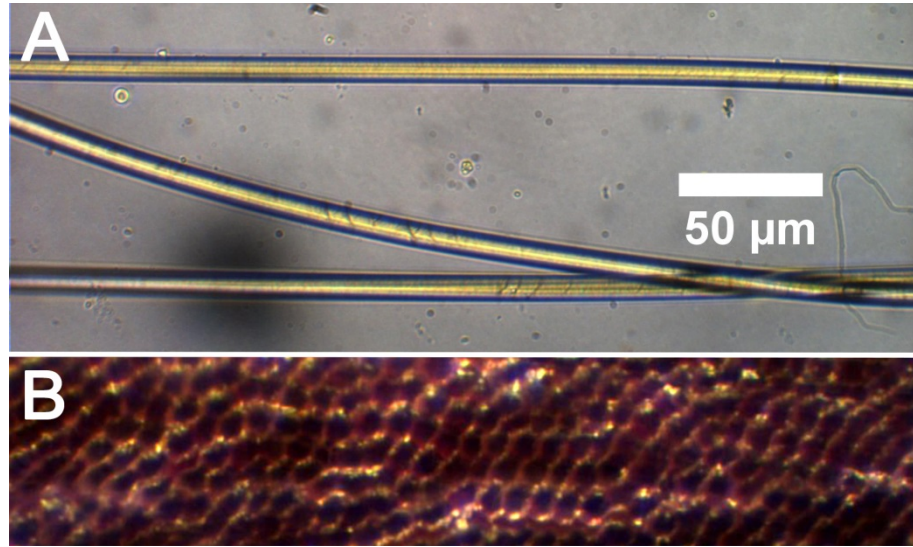


Figure 2.2 Microscope images of Kevlar fiber. **A.** 40X image of filaments. **B.** 20X image of the cross-section of red dye filled fiber

Generally, aramid-family fibers such as aromatic polyamides have extremely high melting temperatures in the range of $\sim 1,100^{\circ}\text{C}$. Among these, Kevlar (DuPont, USA) is a flexible, high strength fiber that is used widely in safety and protection products. Kevlar does not melt but it decomposes at temperatures over 427°C in air. Kevlar demonstrates good wettability as received and its wetting property, and also geometric morphology of interfilament space remain relatively unaffected even after thermal lamination step over 280°C . This fiber is also an inert and biocompatible material that is chemically stable except to strong acids and bases[39]. Kevlar is available as tightly woven fibers composed of thousands of fine single filaments. For this study, we used Kevlar fiber with approximately $600\mu\text{m}$ diameter that is made up 800 filaments and the diameter single filament is $10\mu\text{m}$. Figure 2.2 shows

microscope images of the filaments and a cross-section of its bundle fiber. As shown in images, Kevlar has extremely fine surface roughness and rugosity; hence a longitudinal geometric variation is very low. Excellent geometric homogeneity of fiber is very important because the capillary kinetics is directly determined by this.

2.2.3 LCP film-based Micro Electrode Arrays

The MEA was fabricated using two different types of LCP films. The illustration given in figure 2.3 explains the detailed structure of LCP film-based MEA. First, the electrical interconnections and electrodes were fabricated on low temperature LCP ($T_m=280\text{ }^\circ\text{C}$, $25\mu\text{m}$), and a high temperature LCP ($T_m=315\text{ }^\circ\text{C}$, $25\mu\text{m}$) (Vecstar Series, Kuraray Co., Ltd., Tokyo, Japan) serves as a window layer.

Ti/gold metal films ($1,000\text{Å}/3,000\text{Å}$) were deposited and patterned by sputtering and photolithography on the low temperature LCP film. Soft gold film ($5\mu\text{m}$) was electroplated on the metal pattern. The window layer has well-defined site windows (64 channels) as openings for recording sites and they insulate the electrical lead lines on the circuit substrate layer.

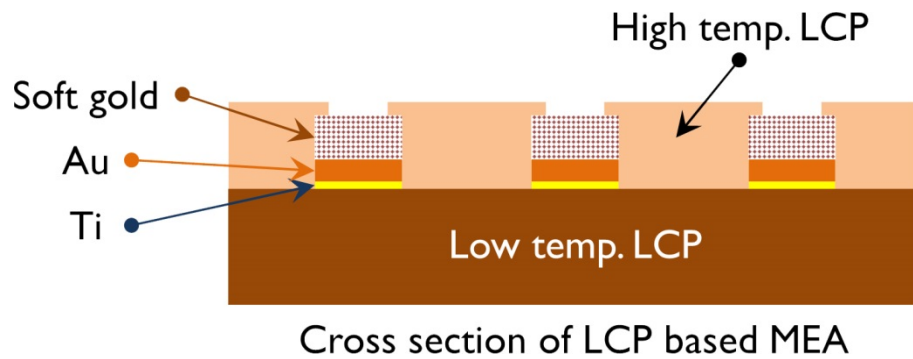


Figure 2.3 Lamination scheme of LCP film-based Micro Electrode Arrays

Typical processing steps require that these two layers are aligned and laminated monolithically using thermal bonding process (300 psi and 280°C for 45 min [15]). The outline of MEA probe was cut to final form using a high intensity UV laser after bonding the metal layer and window layer. The recording/stimulus site of the MEA was cut similar to comb-like shape shown in figure 2.4. This is designed to increase a contact efficiency of electrodes and target tissue. The connector pad in figure 2.5 is designed in perpendicular to main strip of the probe, because fibers must be aligned in a straight line.

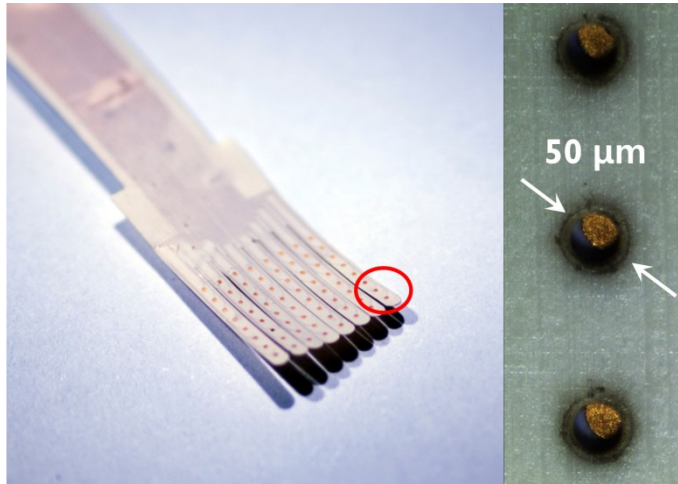


Figure 2.4 Photograph of recording/stimulus electrode of 64 ch. LCP film-based MEA

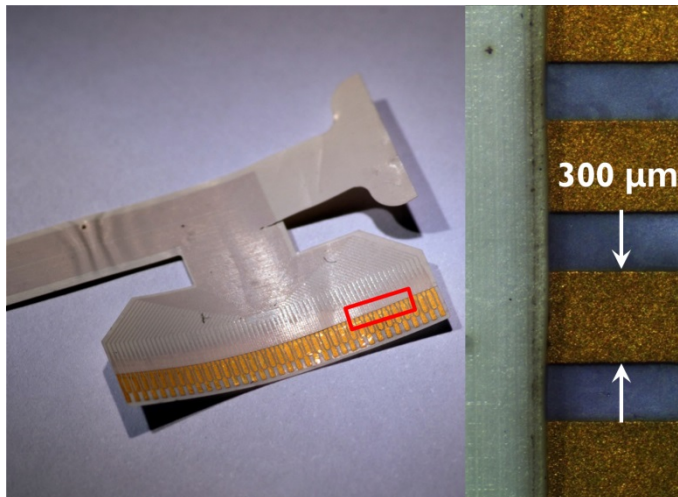


Figure 2.5 Photograph of connector side of 64 ch. LCP film-based MEA

2.3 Integration of fiber-embedded channel and MEA

2.3.1 Design

The integrated probe is made up of three layers of LCP films; 1) cover layer for encapsulation, 2) Kevlar fiber containing guide layer, and 3) MEA containing base layer. The probe was designed with planar 64 channel electrodes for neural prosthesis application. Similar to LCP film-based MEA, additional drug delivery channel is laminated by thermal pressure process. However, heat transfer and pressurization during integration process are spatially selectively applied on the device. To form monolithic implantable probe, thermal bonding was used to integrate drug delivery functioning Kevlar fiber between MEA patterned LCP film and another layer of LCP. A custom aluminum mold was designed and machined provide uniform pressure and directional heating during thermal bonding. Photographs given in figure 2.6 show the in-house aluminum alloy mold for the optimized integration process. Magnified photographs in A of figure 2.6 show an effective contact shape on male mold. Two grooves are aligned not to squash Kevlar fibers and this shape realizes evenly to transfer heat energy and press on multi-layered LCP films.

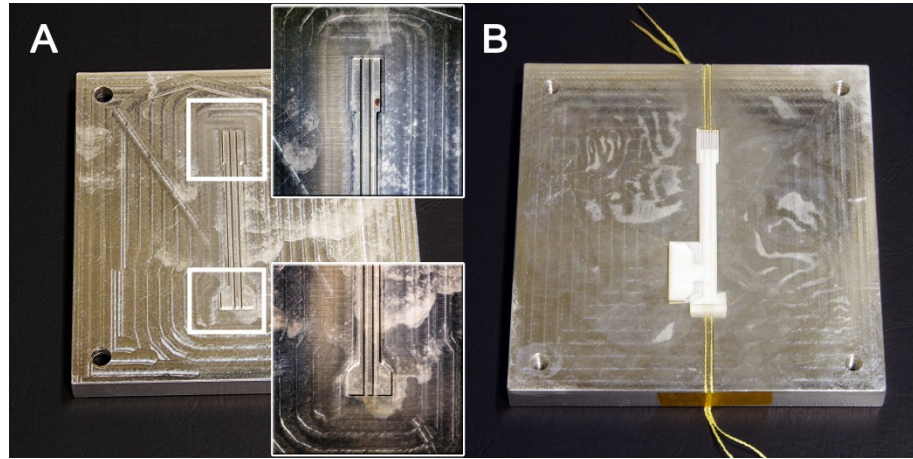


Figure 2.6. Aluminum mold compatible with 64 ch. MEA. **A.** Male mold and partial enlarged images. **B.** Female mold

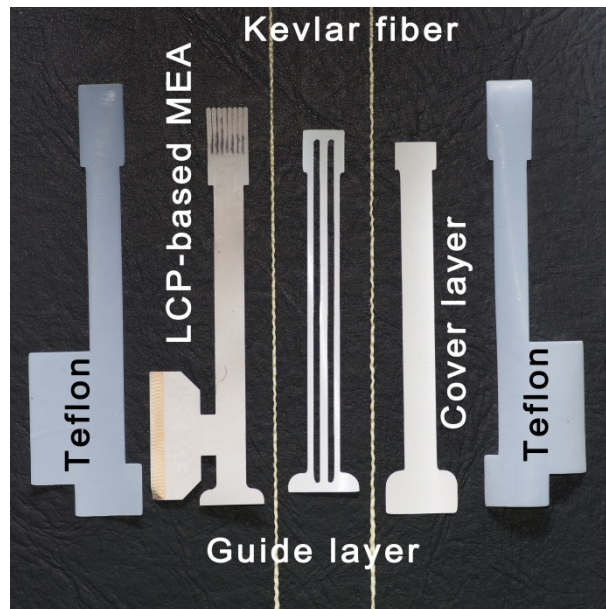


Figure 2.7 Photograph of all components for the flexible neural probe with fiber-embedded drug delivery channel

Each layers and the stacking sequence of layers are shown in figure 2.7 and 2.8, respectively. Kevlar fibers were held in position with a low melting temperature LCP guide layer (50 μ m) placed in the middle. High temperature LCP film (50 μ m, bottom) and electrode patterned LCP film (50 μ m, top) were placed around the Kevlar fibers to form the monolithic probe. The guide layer and bottom cover LCP film were cut with a blade plotter (C330-20, CraftRobo, Japan). Teflon films (100 μ m) were used between the mold and LCP probe to compensate for surface irregularities. Multifilament Kevlar fibers were aligned along grooved lines on the mold, and the tension and twisting number can be adjusted to regulate the flow rate of drug in the channel.

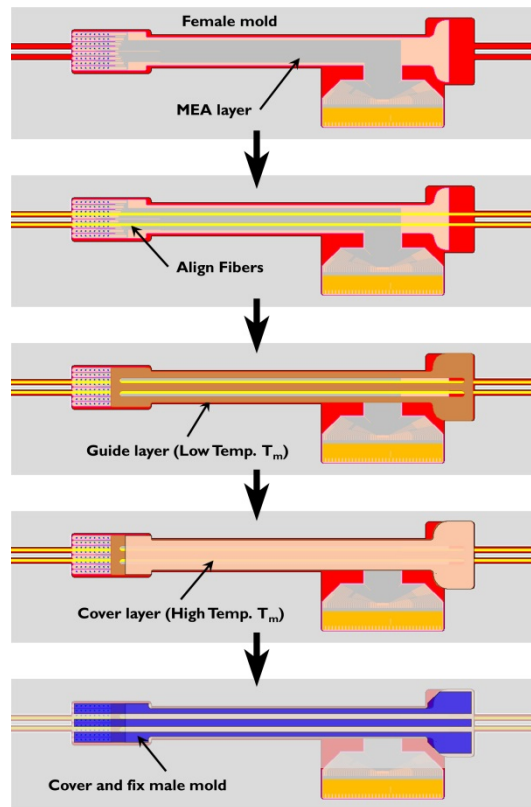


Figure 2.8 Parts lamination sequence for the integration process

2.3.2 Asymmetric thermal pressure lamination process

Because fragile high density metal patterned LCP film need to be thermally bonded to cover LCP film to sandwich Kevlar fibers, slight distortion in pressure or exposure temperature in over LCP melting point can have damaging effect on the electrical performance caused by delamination,

wrinkling or shorting. It is essential that the contact temperature of the MEA patterned LCP film should be kept below 280°C throughout the fabrication process.

To protect the metal electrode patterned layer from high temperature processing, directional heating scheme was used for thermal bonding. Heat source (digital hot plate, PMC, USA) was placed on the bottom and heat sink (heat pipe cooler with 80mm fan) was placed on top while the metal layer containing LCP film was in contact with the heat sink. The top mold in Figure 2.9 should be cooled during the whole process. The optimized temperature ramping profile was plotted in figure 2.9 B. The plotted temperature is the present value of a hot plate. The ramping profile is segmented into three domains of heating and cooling. In the condition of the heat capacity of mold, heat flux of the hot plate and a cooling capacity, the optimal time for heating process is needed over 130 min. After heating step, cooling rate should be tightly controlled because LCP films are susceptible to thermal residual stress. Rapid heating or cooling can cause deformation, delamination or hardening of LCP films and damage the electrodes. Aluminum mold is cooled only by the attached heat sink (opposite the heat source) and the cooling rate ranges from 3.5~5 °C/min. Integration was carried out in a single step over 3 hours period including ramping up and holding the hot plate temperature to 295 °C for 20 min and cooling to room temperature.

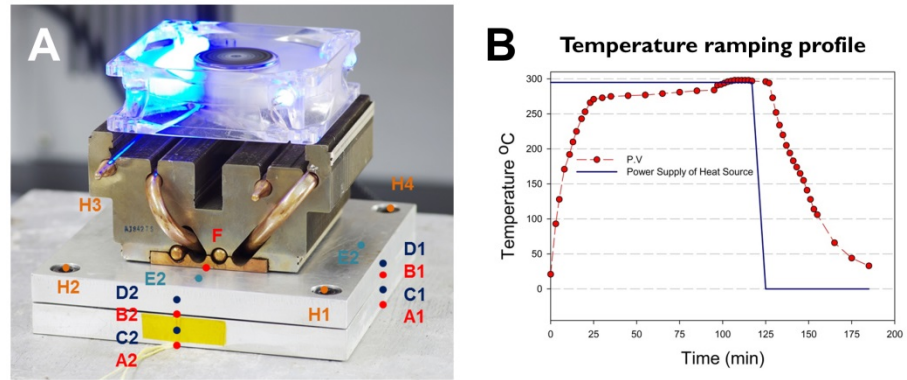


Figure 2.9 Photograph of the asymmetric thermal pressure lamination process and temperature ramping profile

Key point of asymmetric thermal pressure lamination technique is selectively to melt the guide layer of low melting temperature LCP film. It is impossible to measure the inside temperature of mold, directly. To estimate the inside temperature of mold, the steady state temperature of the points shown in figure 2.9 A were measured in the case of cooling and non-cooling. Thermocouple was used to measure the point temperatures and all of data were put into the 3D model of the integration mold in figure 2.10. The measured values of two different cases are listed in table 2.1 and table 2.2, respectively. The estimated temperature value was calculated using boundary element method (BEM), and the graphical analysis images are shown in figure 2.11 and 2.12, respectively.



Figure 2.10 3D rendering image of mold assembly

As the analysis results, maximum temperature of inside is approximately 253°C when cooling activated. While, in case of cooling deactivated, the maximum temperature was estimated 275°C . Although the maximum temperatures of two cases do not exceed the melting temperature of the guide layer LCP, lamination without cooling have been failed. Generally, a melting temperature during a thermal pressure lamination process has a tendency to be lowered than free-load state of film. This is due to a thermal resistance variation by pressure on film layers. The same was founded during the integration process.

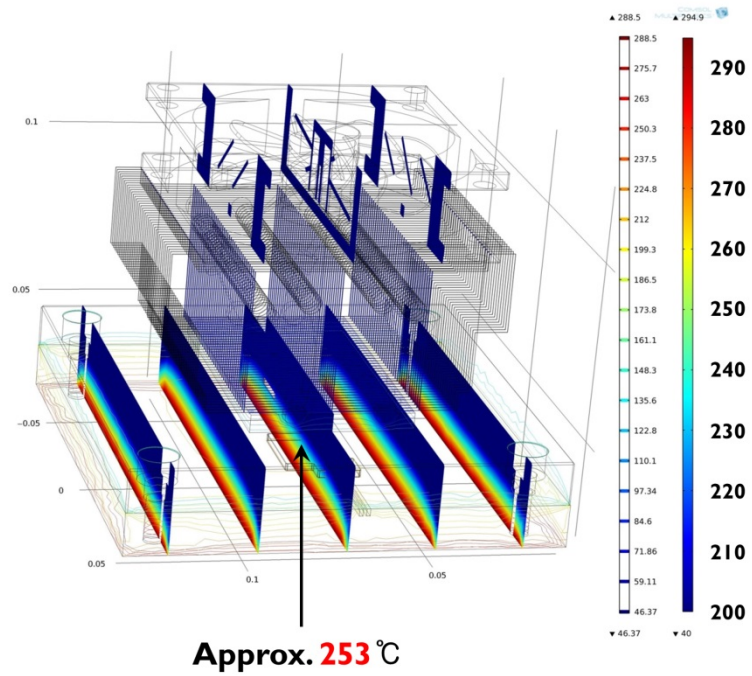


Figure 2.11 Estimation of steady state temperature inside mold with cooling

Table 2.1 Measurement of steady state temperature with cooling condition

	A1	A2	B1	B2	C1	C2	D1	D2	E1	E2	F	H1	H2	H3	H4
Temperature (°C)	295.8	250.0	194.8	179.8	205.5	214.3	135.5	127.5	131.3	127.5	119.3	169.8	170.3	174.5	169.0

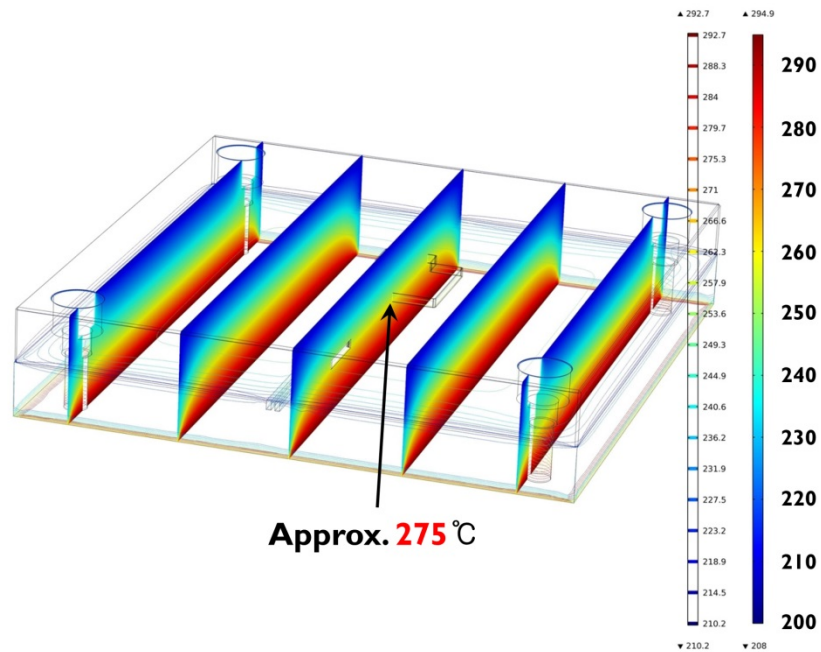


Figure 2.12 Estimation of steady state temperature inside mold without cooling

Table 2.2 Measurement of steady state temperature without cooling condition

	A1	A2	B1	B2	C1	C2	D1	D2	E1	E2	F	H1	H2	H3	H4
Temperature (°C)	295.3	272.8	246.0	252.8	232.0	231.3	212.3	210.3	215.5	201.8	N/A	235.8	237.3	235.8	235.3

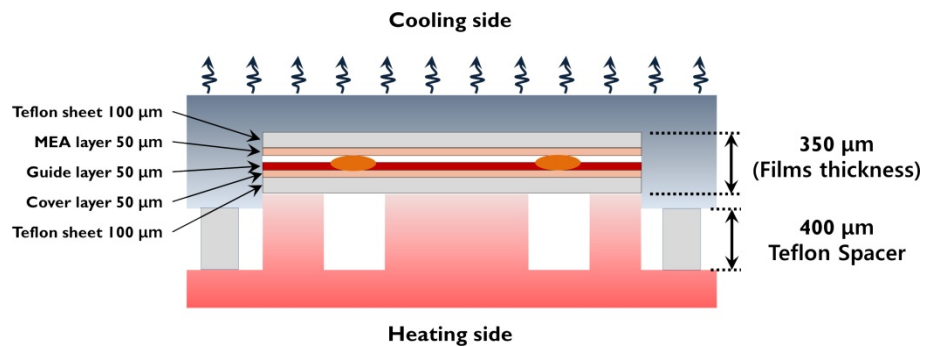


Figure 2.13 Illustration of the assembled mold and components

Application of thermal gradient between top and bottom mold result in selective melting of guide LCP layer that also serves as an adhesive layer between cover and MEA containing LCP films. In addition, guide LCP layer plays a key role in forming void regions around the Kevlar fibers.

Integration process required careful choice of materials to match melting temperatures such that reproducible bonding of each layers were achieved without defects to drug delivery channels and electrodes. For example, if two low temperature LCP layers were used to form fiber-embedded channel, complete melting of the LCP film clogged the fiber channels and penetrated fibers, resulting in non-functional drug delivery channels.

Table 2.3 Integration results according to SV of temperature and pressure condition

SV of hot plate (°C)	Pressurization		Result
	Bolting torque (kg·f)	Effective pressure(psi)	
< 295	0.15~0.30	243~265	· Bonding failure
292~295			· Monolithic bonded
> 295			· Shrinkage of film · Delamination of metal wiring
292~295	< 0.15	< 243	· Bonding failure
	> 0.30	> 265	· Tearing · Burying of fiber into film

A custom aluminum press mold was designed to provide uniform pressure and directional heating during thermal bonding. Figure 2.13 shows a schematic of the integration method. Laminating pressure is indirectly controlled with bolting torque at four points around the corners. The total thickness of probe (including MEA patterned LCP, Kevlar fiber/LCP guide layer, and bottom cover LCP layers) is 150µm. Additionally, two sheets of Teflon (100µm) were inserted between the mold, and a 400µm thick Teflon spacer was placed around the probe periphery. This allowed positive thickness margin of 50µm before application of bolting torque in the range of 0.15~0.30 Kgf·m and the measured effective pressure were listed in table 2.3.

Various results according to temperature and the applied bolting torque were listed in table 2.3. Lower temperature below 292°C results in bonding failure of

each LCP layers and higher temperature over 295°C results in physical damages on films. For examples, shrinkage of film and/or delamination of metal wiring occurred when over-heating conditions. In over-pressure cases, tearing of the window layer with 25µm-thickness was founded and Kevlar fibers were buried in cover layer with 5µm-thickness

2.2.3 Electrical features of the integrated device

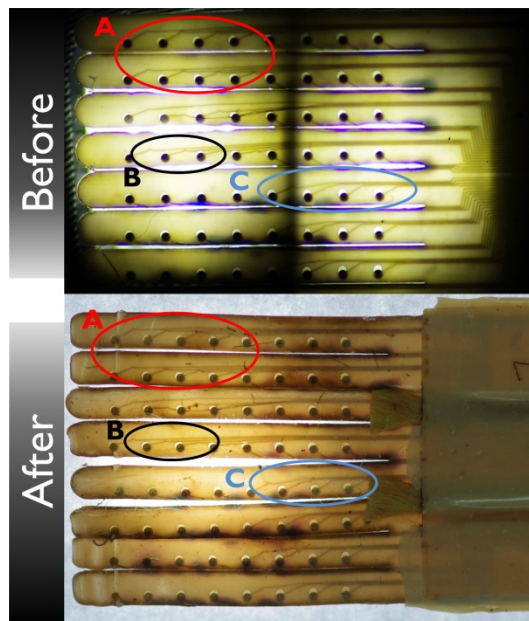


Figure 2.14 Comparison of wiring state on recording/stimulation site before and after integration process

Prior to measurement, the metal wiring section and the recording sites were inspected by optical microscopy. Optical inspection confirmed that metal interconnect patterns are intact and do not show distortions or damage after the bonding process. Buried electrodes/interconnects can be observed under the cover LCP layer in figure 2.14. The width of the covered interconnections is $10\mu\text{m}$ with $50\mu\text{m}$ spacing and the diameter of opening in the window layer for the electrode is $150\mu\text{m}$. All electrodes and interconnections maintained initial aligned state and no visible damages were observed. Two photographs A and B given in figure 2.14 indicate an optical comparison result of the buried metal wiring before and after integration process. Photograph of the cross-section of the probe (shown earlier in Figure 2.1) clearly show the metal interconnects positioned adjacent to the embedded Kevlar fibers. These interconnect are not affected by the lateral deformation of the LCP substrate film during the thermal bonding step. The window layer that covers the recording site also does not show signs of deformation.

Impurities on the recording sites were removed with air plasma treatment (for 30min at 50W). The integrated devices were connected to an impedance analyzer (Solartron, SI 1287/SI 1260, Durham, UK). Recording site was immersed in phosphate buffered saline (PBS, pH 7.4, 1X) with an Ag/AgCl reference electrode. Impedance and phase angles were acquired from 10 Hz to 100 kHz for each channel.

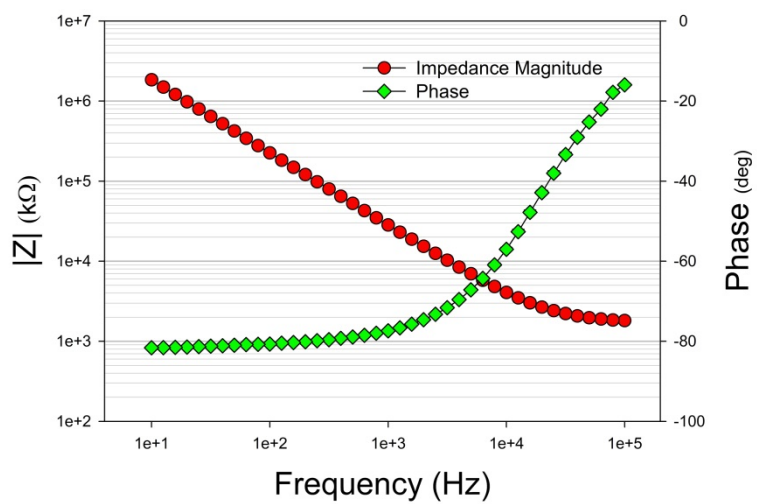


Figure 2.15 Impedance spectroscopy of the 64 ch. electrodes after integration process

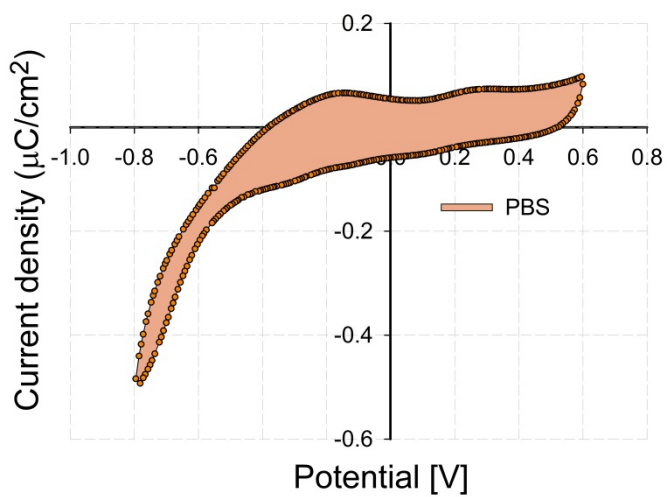


Figure 2.16 Measured cyclic voltammetry of Au electrode site in phosphate buffered saline (PBS) at 50 mV/s

Cyclic voltammetry was measured with the same three-electrode composition as the impedance spectroscopy measurement. CV identifies the electrochemical characteristics such as the reversibility of the reactions, the quantity of electroactive material on the electrode, and the stability of the electrode during conventional electrical stimulation process. The charge storage capacity (CSCc) is calculated from the time integral of the cathodic current level in a slow-sweep-rate CV over a potential in the water-window-range of 1X phosphate buffered saline. The CSCc means the total available amount of charge for a stimulation pulse[40]. For 64 electrodes, the obtained time integral of CSCc is $65.33 \pm 0.25 \mu\text{C}/\text{cm}^2$ and this value is sufficient to stimulate various nerve system including motor cortex [40].

2.3.4 Results and discussion

The key point of the fiber integration process is to preserve the metal electrode network on the pre-made LCP film-based MEA and to preserve electrical integrity. Because fragile high density metal patterned LCP film need to be thermally bonded to cover LCP film to sandwich Kevlar fibers, slight distortion in pressure or exposure temperature in over LCP melting point can have damaging effect on the electrical performance caused by delamination, wrinkling or shorting. As the result of temperature estimation using BEM, it is essential that the contact temperature of the MEA patterned LCP film should be kept below 253°C throughout the fabrication process.

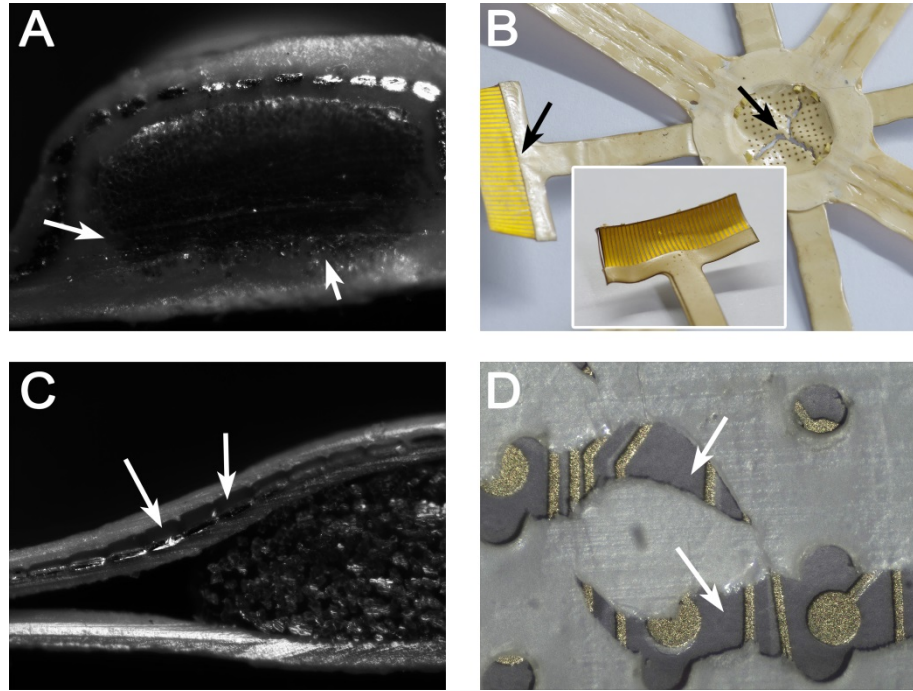


Figure 2.17 Examples of defective devices due to over- heating and/or over pressure

Figure 2.17 shows various examples of defective samples due to abnormal integration condition. Temperature and also pressure conditions have to correspond with the optimized ranges, respectively. The maximum limit of inside temperature of mold was numerically estimated.

Chapter III

Study of drug delivery performance

3.1 The capillary kinetics in Kevlar fiber

3.1.1 The capillary kinetics of pre-wetted and dry Kevlar fiber

As a preceding research, the capillary kinetics in Kevlar fiber has been investigated. Generally, vertical capillary flows have been well characterized in hollow structures; they follow the Washburn law[41], which explains the balance between the velocity and the Poiseuille profile, as expressed below

$$\frac{dh}{dt} = \frac{R^2}{8\mu} \left[\frac{2\gamma \cos \theta}{Rh} - \rho g \right] \quad (1)$$

Here, the liquid height h is a function of time t , the capillary radius is R , the dynamic viscosity is μ , the surface energy is γ , and the contact angle is denoted as θ . The inertia term ρg is negligible in surface energy term;

thus, the height h can be extended to account for the length as well. With assumptions of some of variables such as an infinitesimal quantity of liquid and the Taylor expansion, Eqn. (1) can be rewritten as follows:

$$h \sim \left(\frac{\rho g R^2 H_0}{4\mu} \right)^{1/2} \sqrt{t} \quad (2)$$

here, H_0 is the maximum length of the capillary flow, and the capillary flow rate is proportional against the square root of time t .

First, we investigated the difference of capillary kinetics of pre-wetted and dry Kevlar fibers. To simulate a fiber condition after the thermal bonding step, Kevlar fibers we used were heated to 280°C on a hot plate for 1 hour and cooled naturally. A 10µl droplet of red dye solution was placed at the end of the fibers without tension and twisting. Time-lapse images were taken using a DSLR (K-5 IIs, Pentax, Japan) camera with a 100-mm macro lens at one-second interval. Time-lapse images with one second interval were converted using max entropy thresholding method in red color space, and thus we measured the capillary length in time domain. The capillary length was measured and averaged for five different samples and the capillary wicking distance (distance that red dye travelled) is plotted in figure 3.1. The soaking behavior of the dry Kevlar follows Washburn law which describes the balance between the velocity and Poiseuille profile[41]. Compared to dry fibers, pre-

wetted Kevlar fiber shows longer wicking distance that is as much as two times longer. Furthermore, the flow speed on pre-wetted fiber is nearly constant from the start. We therefore used pre-wetted conditions for further experiments.

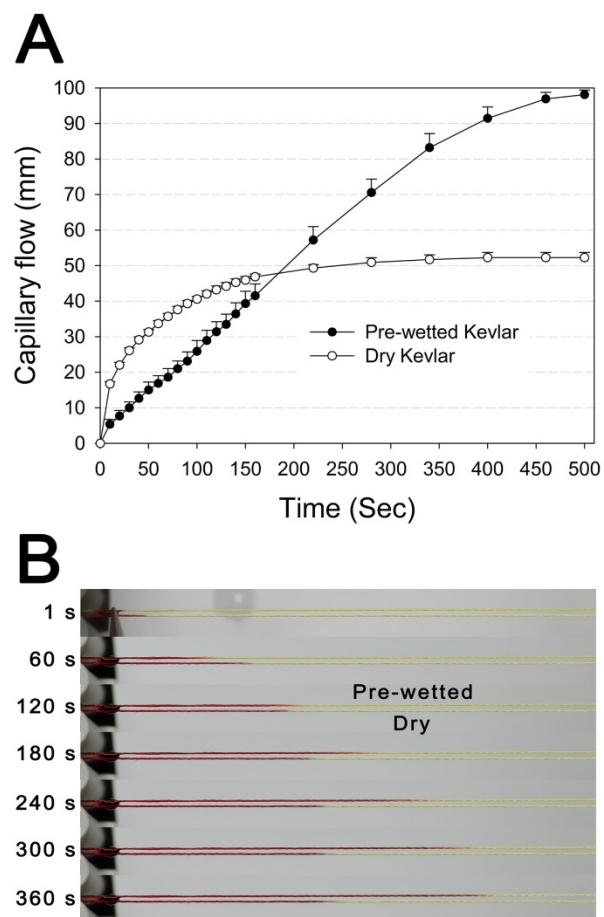


Figure 3.1 The capillary kinetics of pre-wetted and dry Kevlar fiber

3.1.2 The capillary kinetics of various geometric variation of fiber

To characterize the capillary kinetics according to various geometric conditions of Kevlar fiber, tension and twist number per unit length were adjusted.

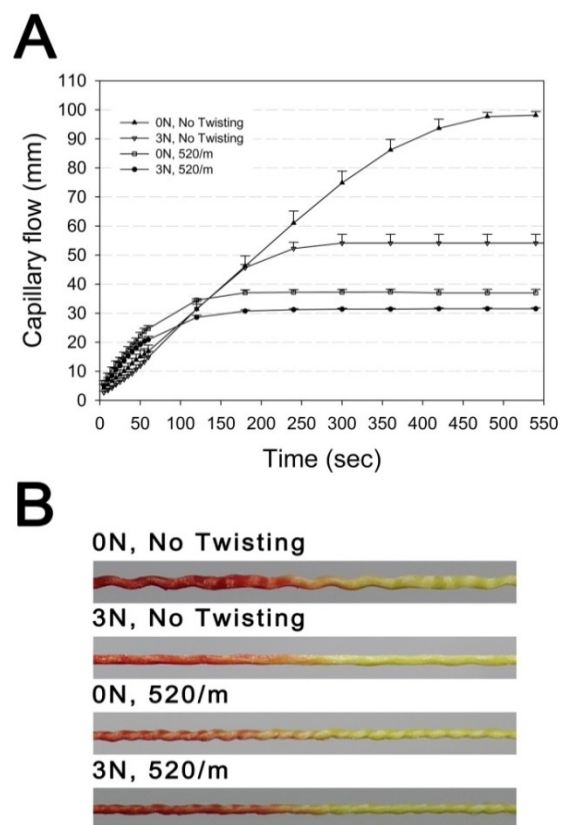


Figure 3.2 The capillary kinetics of various conditions of fiber

Over 3N without twisting, coaxial porosity of Kevlar we used asymptotically converges to 0.55. In the case of twisting over 600/m, Kevlar fiber was entangled by itself, and thus the geometrical heterogeneity along fiber became an artifact. As this result, we determined the maximum tension and twisting number as 3N and 520/m, respectively. One of the variables associated with the capillary kinetics of flow in fiber is a geometrical factor of the interfilament space such as rugosity, coaxial porosity and perimeter of cross section of fiber bundle. As mentioned above, single filament of Kevlar shown in figure 2.2 has extremely fine longitudinal smoothness and coaxial circularity; hence heterogeneity of interfilament space is negligible. The coaxial porosity of Kevlar can be calculated by $P = 1 - \frac{r^2 \cdot N}{R^2}$, where N the number of filaments, r and R are the diameter of filament and fiber bundle, respectively. Kevlar fiber used in the channel is approximately made up of 800 single filaments of 10 μm diameter. We took the picture of each fiber bundle using macro lens and measured statistically averaged diameter of 20 samples, respectively.

Figure 3.2 shows the capillary flow of four different conditions of fiber which are pre-wetted. Capillary speed of initial stage represents linearity due to the effect of pre-wetted surface of fiber. The graph given in figure 3.3 indicates that capillary flow resistance is directly related to a change of coaxial porosity by tension and twisting. Filament number of fiber bundle determines cross-sectional perimeter which is related to surface tensional force at the meniscus of liquid front. Coaxial porosity is the portion of empty cross-sectional area. In fibers with same number of filaments, lower coaxial

porosity means increment of capillary flow resistance due to decrease of coaxial interfilament area. This simple mechanism can be applied to regulate an overall flow rate of a fiber embedded fluidic channel. A simple illustration given in figure 3.31 of next chapter is a model of drug-fiber channel-target tissue. When a fiber is sandwiched with a minimum flow resistance R_E (no tension, no twisting), overall flow resistance might be regulated below R_E by adjusting a fiber at inlet side. In addition, capillary flow resistance can be affected by twisting of fiber[42]. In the horizontal wicking model in porous fiber, the movement of the liquid is determined by capillary force, viscous drag and inertia. Among these forces, capillary force in twisted fiber can be defined by positive force F_p due to the interaction between the liquid and the fibers and negative force F_n due to the concave liquid-gas interface[43-45]. Therefore,

$$F_C = F_p - F_n, \quad (3)$$

$$F_C = \frac{4\pi\phi\gamma_{LS}}{\rho_f \bar{r}_f} \int_0^r \frac{H}{\sqrt{H^2 + 4\pi^2 r_F^2}} \cdot r_F \cos(\theta_a + \alpha) dr_F - \phi 2\pi r_f \gamma_{LG}, \quad (4)$$

where ϕ is packing fraction of fiber in the bundle, r is the outer radius of the fiber, ρ_f is cross-sectional filament density, \bar{r}_f is filament radius, θ_a is advancing contact angle between the liquid and the fiber and α is the helix angle of

filaments. H is the pitch length and $\sqrt{H^2 + 4\pi^2 r_F^2}$ means the trajectory length of one period, respectively. Two terms in integrand of equation (4), $H/\sqrt{H^2 + 4\pi^2 r_F^2}$ and $\cos(\theta_a + \alpha)$ were added due two twisting effect. In mathematically, two terms in integrand $H/\sqrt{H^2 + 4\pi^2 r_F^2}$ and $\cos(\theta_a + \alpha)$ always less than 1 and $\cos\theta_a$, respectively. That means that the capillary driving force in twisted fiber is less than the force in a straight fiber when the fibers have same coaxial porosity.

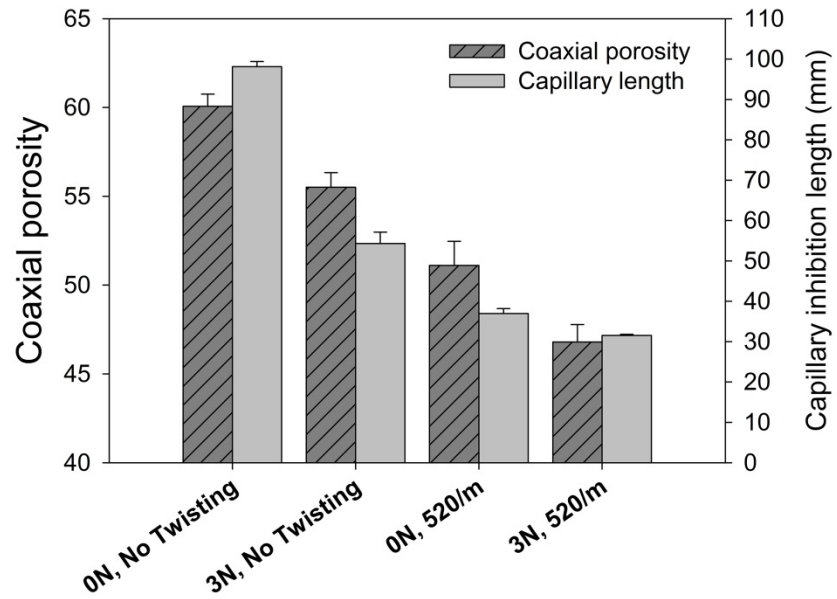


Figure 3.3 Coaxial porosity and capillary inhibition length according to various conditions of fiber

3.2 Drug diffusion dynamics in agarose gel

When a fiber-embedded drug delivery channel is implanted into a brain, drug diffusion behavior and profile are important factors because a design of drug release ports on a device has to be determined by considering diffusive characteristics. Using agarose gel as a surrogate of human brain tissue, many research groups have reported various drug diffusion characteristics in theoretical and experimental approaches. However, most of earlier studies are based on diffusibility of injected drug but the drug delivery mechanism of our approach is different from a conventional injecting system [46-53].

In this part, we have described a liquid diffusion behavior in 1% agarose gel. In a view point of drug or liquid, Kevlar fiber as a drug delivery pipeline might be considered as an absorber. Similar to this, agarose gel as a brain phantom is also an absorber. At the interface of fiber and brain, an absorptivity difference of each porous material results in the inherent diffusion characteristics of drug.

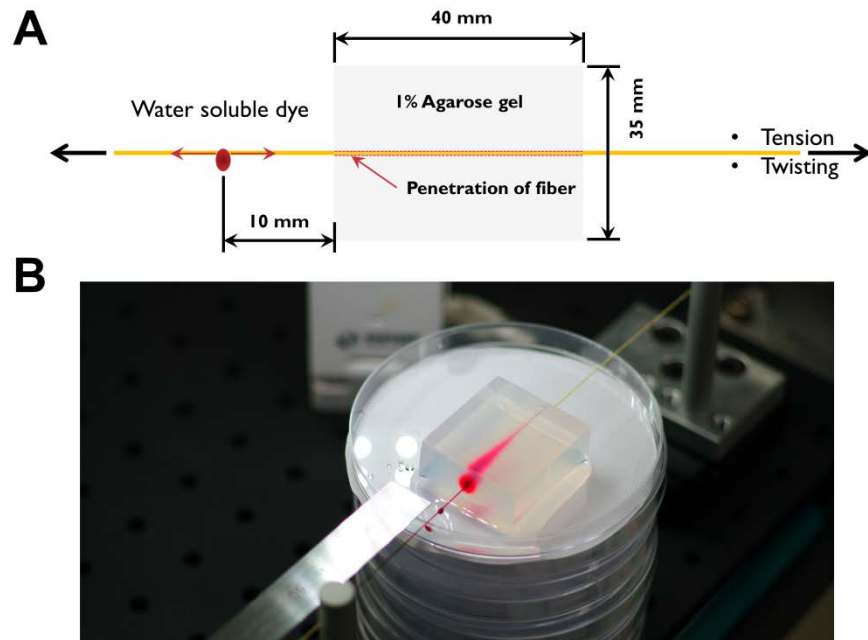


Figure 3.4 Illustration and photograph of experiment setup

We use also 1% agarose gel as a surrogate of brain, and Kevlar fiber was penetrated a section of agarose gel block with various geometric variations same to previous conditions. To eliminate experimental artifacts such as bubble around fiber and/or a gap at the fiber-agarose gel interface, agarose gel was compressed slightly. Figure 3.4 shows the experimental procedure and setup. Water soluble red dye was supplied on 10 mm point from an agarose gel wall and time-lapse images with ten seconds interval were taken over 30 minutes using DSLR camera with 100 mm macro lens. For an equalized intensity of red dye, spatial mean illuminance of the image ROI was fixed in accordance with -1.0 eV at f 7.1 and 1/10 second.

3.2.1 Physical and mathematical modeling

The diffusion in agarose gel given in figure 3.4 is conical shape along the penetrated fiber. Transported liquid via fiber is split into two ways of a circumferential agarose gel and frontal section of capillary front. We assumed some of physics like below.

- (1) The kinetics of a spherical diffusion behavior at arbitrary point of fiber is independent.
- (2) Coefficient of a spherical diffusion from fiber to agarose gel is dependent on a spatial concentration of liquid at arbitrary point of fiber.
- (3) Diffusion in agarose gel and wicking of fiber agree Washburn law, proportional to root of elapsed time.
- (4) A split ratio τ of liquid in fiber is constant along fiber.

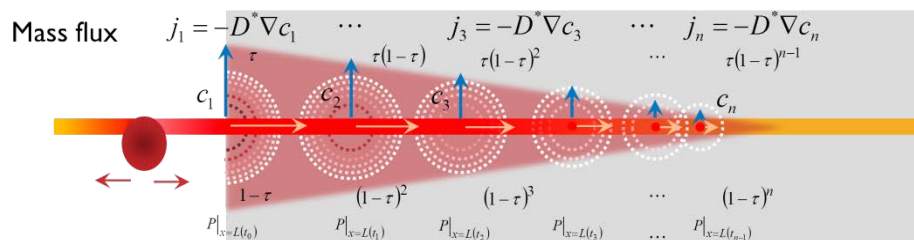


Figure 3.5. Physical modeling of the diffusion behavior in agarose gel

By means of the assumption, liquid diffusion behavior in agarose gel was simplified like figure 3.5. Red point given in figure 3.4 indicates the location of capillary front when elapsed time t_n and the concentric circles are the diffusion front traces in time-domain. Diffusion modeling is postulated physically similar to Huygens law which explains a wave propagating phenomenon, because red points are considered as point sources of diffusion. For a phenomenological approach, split ratio τ ($0 \leq \tau \leq 1$) was assumed and it means absorptivity of agarose gel against the penetrated fiber. If the ratio τ is constant at any position, the diffused fraction from any time point $P|_{x=L(t_i)}$ might be $\tau(1-\tau)^{i-1}$. Similarly, the residue fraction on capillary front can be denoted as $(1-\tau)^i$. By Fick's law, mass flux by diffusion in porous media was defined by the multiply of the effective diffusivity and the negative gradient of concentration of diffusing molecules, $j_i = -D^* \nabla C$ [49]. Therefore the diffusive driving force of time points $P|_{x=L(t_i)}$ decreases with increasing time step i and this approach allows $\alpha_n(x)$ to be estimated numerically in an attenuation form against position x . In this research, $\alpha_n(x)$ was expressed as an exponential function like equation (4) because of two reasons. First, exponential function is a representative function which is always positive against x . And the R value of regression fitting of this form is reasonable compared with linear, polynomial fitting curves.

Length of the capillary front (or penetration length) in fiber is a function of time and thus it can be expressed $L(t_n)$. Hence, we can define that the radius of

spherical diffusion front at point $L(t_n)$:

$$R_n(x, t) = \alpha_n(x) \cdot \sqrt{t} \cdot H(t - t_n) \quad (5)$$

where $\alpha_n(x)$ is a coefficient of lateral diffusion, H is Heaviside function to regulate time delay of diffusion. $\alpha_n(x)$ is a function of coordinate x , whereas variable x in $\alpha_n(x)$ means the length $L(t_n)$ of the capillary front at t_n . Additionally, if we assume that $\alpha_n(x)$ is exponentially decay according to $x = L(t_n)$, equation (5) is rewritten:

$$R(t) = \alpha_0 \cdot e^{-L(t_n)/\xi} \cdot \sqrt{t} \cdot H(t - t_n) \quad \text{at the capillary front when } t_n \quad (6)$$

where α_0 is a coefficient of spherical diffusion at $x_0 = L(t_0)$ and ξ is a longitudinal attenuation factor of α . Consequently, equation (6) is decomposed into the coordinate term and the radius of spherical diffusion front against time.

3.2.2 Experimental data

The geometric variation of Kevlar fiber is applied equally to previous experiment. Time-lapse image data was acquired at least five times against fiber condition, and the three data sets were sampled excluding data set with high variance. Time-lapse images were stacked and the moment when red dye in Kevlar fiber touched the wall of agarose gel block was set as the zero point in time domain. To estimate the coefficients of equation (6), $L(t_n)$ and $R_n(x,t)$ were measured in millimeter (mm) scale. For an consistency of measured values of $L(t_n)$ and $R_n(x,t)$, whole stacked data were converted using the max entropy thresholding algorithm, which is one of the useful algorithm for segmentation purpose[50]. Figure 3.6 shows an original and a converted image. The merged image given in right of figure 3.6 implies excellent identity of converted images.

Capillary length $L(t_n)$ in fiber was measured from the zero point of time and spatial domain. The result was plotted in figure 3.7 and regression curve was calculated in minute scale without time shifting.

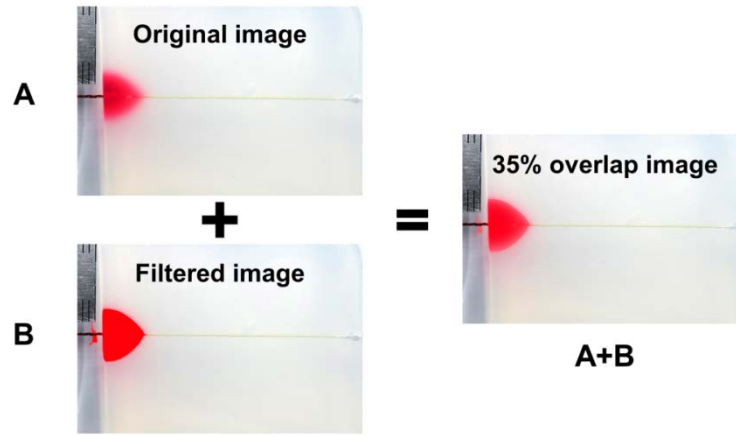


Figure 3.6 An example of a filtered image using the max entropy thresholding method

However, the radius of spherical diffusion $R_n(x,t)$ needs specific position of x . Capillary inhibition length in fiber were divided equally into 4~5 parts. As a result, measurement points of no twisting cases (relatively higher coaxial porosity) were determined around 0, 5, 10, 15, 20 mm and 0, 3, 6, 9, 12 mm from the origin of longitudinal axis, respectively. In 520/m twisting case (low coaxial porosity), the points were determined around 0, 1, 2, 3, 4 mm from the origin. Furthermore t_s , an elapsed time when a capillary front reaches on each measurement points, has a variance. To minimize curve fitting error by time shifting at the measurement points, $R_n(x,t)$ were plotted individually by samples and regression coefficients of $R_n(x,t)$ were calculated in second scale.

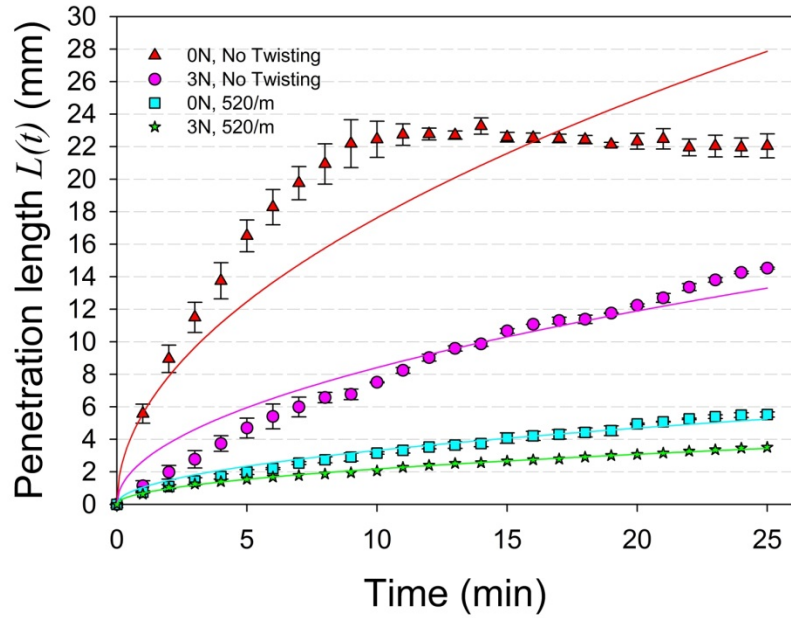


Figure 3.7 The kinetics of capillary front against time

Table 3.1 Regression coefficients l_{FC} and R value of the penetration length against t (min)

Fiber condition		Regression coefficient $L(t) = l_{FC}\sqrt{t}$	R
Tension (N)	Twisting (rotate/m)		
0	No	5.57	0.8099
3		2.66	0.9727
0	520	1.05	0.9863
3		0.69	0.9983

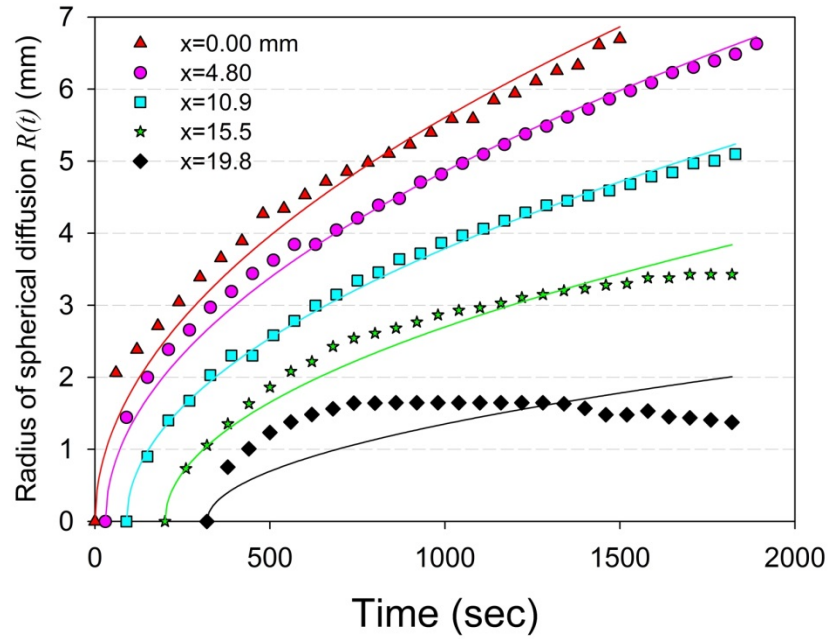


Figure 3.8 Plot of the diffusion radius R against t and x . Sample no.1 without tension and twisting

Table 3.2 Regression functions α_x and R value of sample no.1 without tension and twisting

Fiber condition	Sample	Measurement point (mm)	Regression curve $R_x(t) = \alpha_x \sqrt{t - t_s}$	R
No Tension No Twisting	No.1	0.00	$0.1772\sqrt{t}$	0.9867
		4.80	$0.1560\sqrt{t - 30}$	0.9960
		10.9	$0.1255\sqrt{t - 90}$	0.9981
		15.5	$0.0954\sqrt{t - 200}$	0.9729
		19.8	N/A	N/A

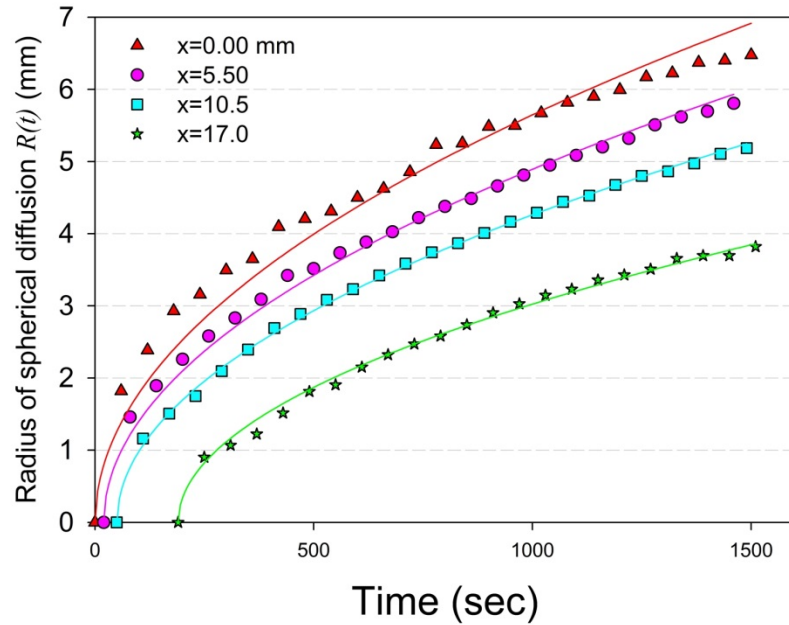


Figure 3.9 Plot of the diffusion radius R against t and x . Sample no.2 without tension and twisting

Table 3.3 Regression functions α_x and R value of sample no.2 without tension and twisting

Fiber condition	Sample	Measurement point (mm)	Regression curve $R_x(t) = \alpha_x \sqrt{t - t_s}$	R
No Tension No Twisting	No.3	0.00	$0.1785\sqrt{t}$	0.9844
		5.50	$0.1563\sqrt{t - 20}$	0.9971
		10.5	$0.1383\sqrt{t - 50}$	0.9995
		17.0	$0.1062\sqrt{t - 190}$	0.9976

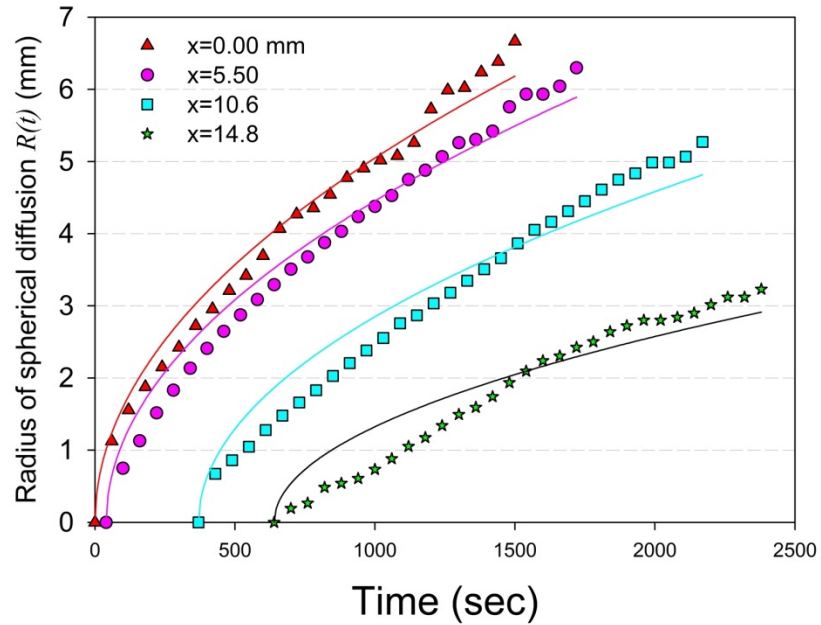


Figure 3.10 Plot of the diffusion radius R against t and x . Sample no.3 without tension and twisting

Table 3.4 Regression functions α_x and R value of sample no.3 without tension and twisting

Fiber condition	Sample	Measurement point (mm)	Regression curve $R_x(t) = \alpha_x \sqrt{t - t_s}$	R
No Tension No Twisting	No. 3	0.00	$0.1596\sqrt{t}$	0.9908
		5.50	$0.1437\sqrt{t - 40}$	0.9889
		10.6	$0.1135\sqrt{t - 370}$	0.9740
		14.8	$0.0698\sqrt{t - 640}$	0.9435

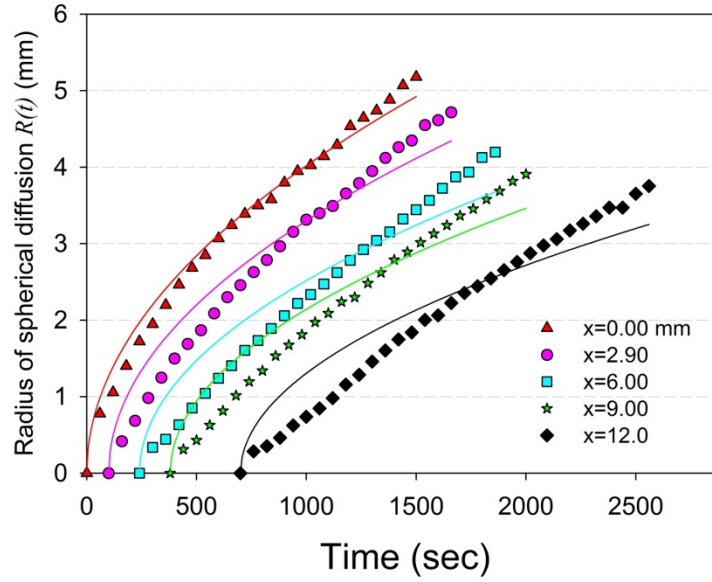


Figure 3.11 Plot of the diffusion radius R against t and x . Sample no.1 with 3N tension and without twisting

Table 3.5 Regression functions α_x and R value of sample no.1 with 3N tension and without twisting

Fiber condition	Sample	Measurement point (mm)	Regression curve $R_x(t) = \alpha_x \sqrt{t - t_s}$	R
3N No Twisting	No. 1	0.00	$0.1271\sqrt{t}$	0.9932
		2.90	$0.1100\sqrt{t - 100}$	0.9761
		6.00	$0.0913\sqrt{t - 240}$	0.9559
		9.00	$0.0860\sqrt{t - 380}$	0.9603
		12.0	$0.00754\sqrt{t - 700}$	0.9487

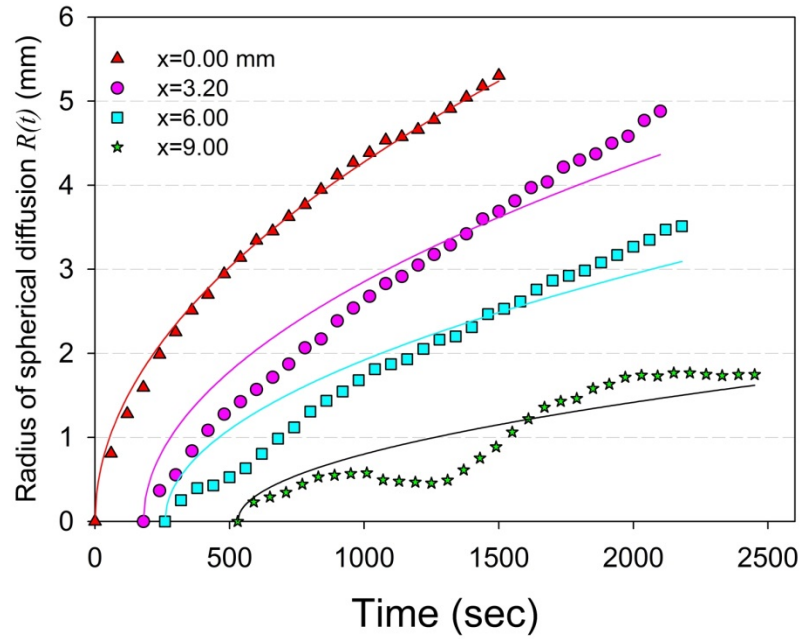


Figure 3.12 Plot of the diffusion radius R against t and x . Sample no.2 with 3N tension and without twisting

Table 3.6 Regression functions α_x and R value of sample no.2 with 3N tension and without twisting

Fiber condition	Sample	Measurement point (mm)	Regression curve $R_x(t) = \alpha_x \sqrt{t - t_s}$	R
3N No Twisting	No.2	0.00	$0.1352\sqrt{t}$	0.9980
		3.20	$0.0996\sqrt{t - 180}$	0.9703
		6.00	$0.0706\sqrt{t - 260}$	0.9539
		9.00	$0.0370\sqrt{t - 530}$	0.8884

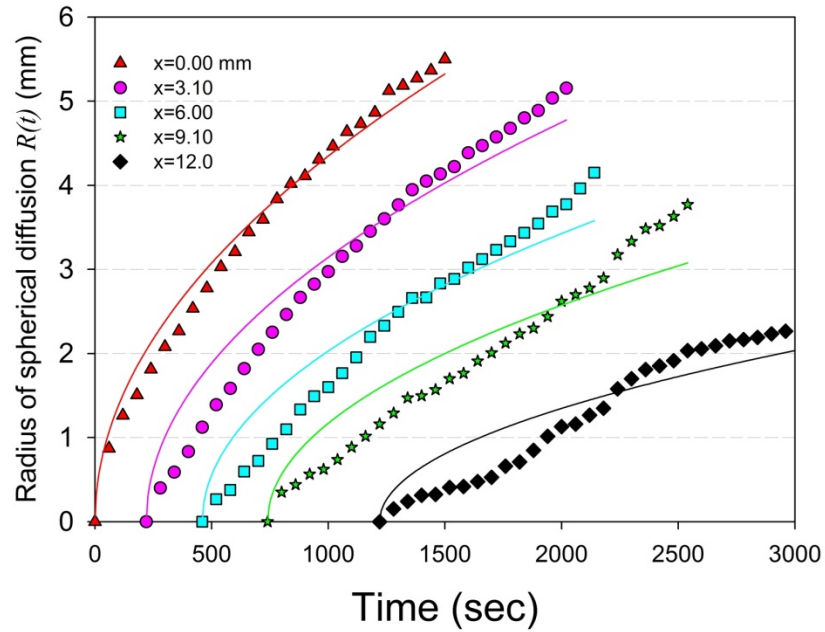


Figure 3.13 Plot of the diffusion radius R against t and x . Sample no.3 with 3N tension and without twisting

Table 3.7 Regression functions α_x and R value of sample no.3 with 3N tension and without twisting

Fiber condition	Sample	Measurement point (mm)	Regression curve $R_x(t) = \alpha_x \sqrt{t - t_s}$	R
3N No Twisting	No.3	0.00	$0.1375\sqrt{t}$	0.9920
		3.10	$0.1126\sqrt{t - 220}$	0.9738
		6.00	$0.0873\sqrt{t - 460}$	0.9557
		9.10	$0.0725\sqrt{t - 740}$	0.9362
		12.0	$0.0482\sqrt{t - 1220}$	0.9139

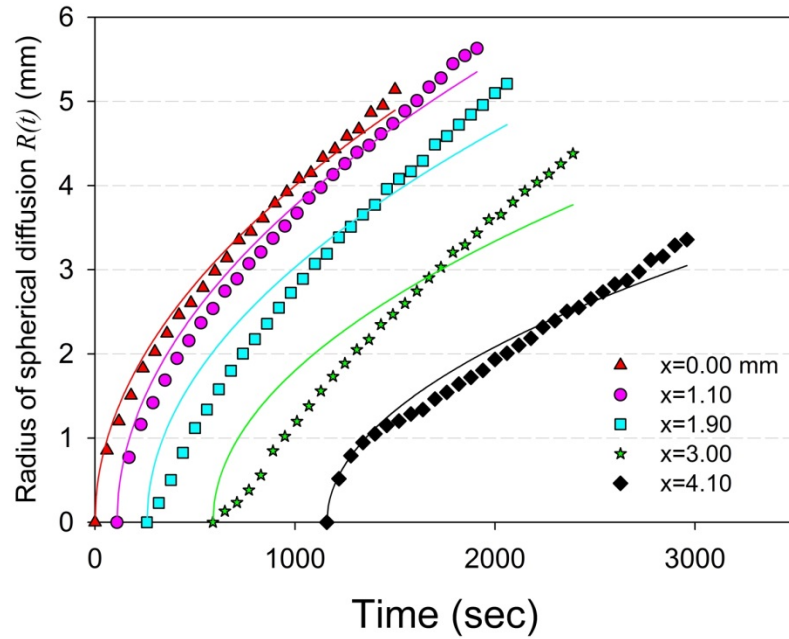


Figure 3.14 Plot of the diffusion radius R against t and x . Sample no.1 without tension and with twisting of 520/m

Table 3.8 Regression functions α_x and R value of sample no.1 without tension and with twisting of 520/m

Fiber condition	Sample	Measurement point (mm)	Regression curve $R_x(t) = \alpha_x \sqrt{t - t_s}$	R
No tension 520/m	No.1	0.00	$0.1264\sqrt{t}$	0.9958
		1.10	$0.1261\sqrt{t - 110}$	0.9929
		1.90	$0.1113\sqrt{t - 260}$	0.9683
		3.00	$0.0889\sqrt{t - 590}$	0.9398
		4.10	$0.0719\sqrt{t - 1160}$	0.9838

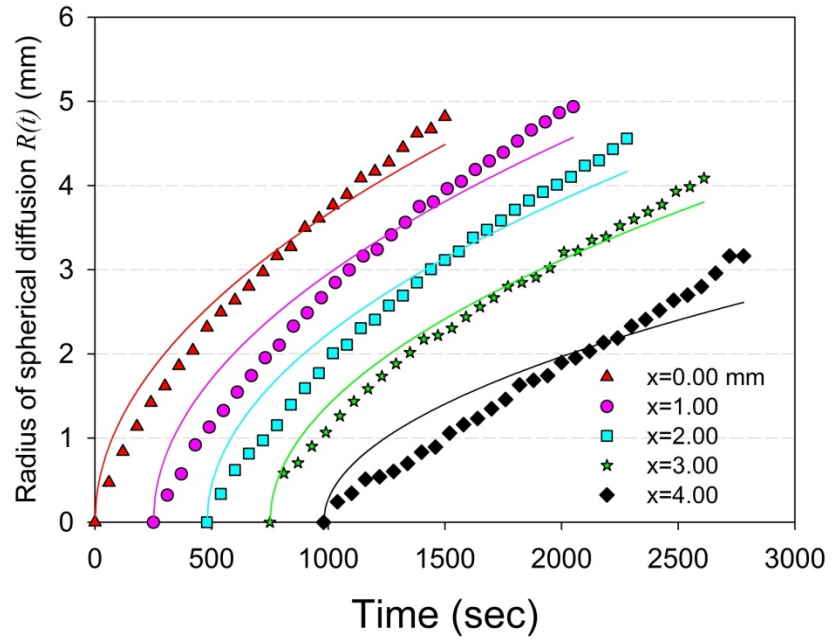


Figure 3.15 Plot of the diffusion radius R against t and x . Sample no.2 without tension and with twisting of 520/m

Table 3.9 Regression functions α_x and R value of sample no.2 without tension and with twisting of 520/m

Fiber condition	Sample	Measurement point (mm)	Regression curve $R_x(t) = \alpha_x \sqrt{t - t_s}$	R
No tension 520/m	No.2	0.00	$0.1159\sqrt{t}$	0.9822
		1.00	$0.1078\sqrt{t - 250}$	0.9735
		2.00	$0.0982\sqrt{t - 480}$	0.9735
		3.00	$0.0882\sqrt{t - 750}$	0.9883
		4.00	$0.0616\sqrt{t - 980}$	0.9384

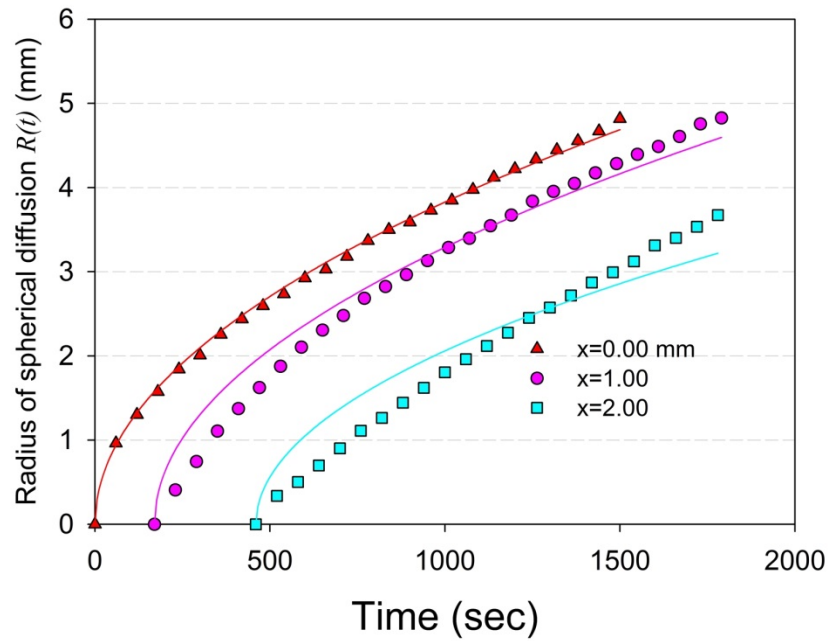


Figure 3.16 Plot of the diffusion radius R against t and x . Sample no.3 without tension and with twisting of 520/m

Table 3.10 Regression functions α_x and R value of sample no.3 without tension and with twisting of 520/m

Fiber condition	Sample	Measurement point (mm)	Regression curve $R_x(t) = \alpha_x \sqrt{t - t_s}$	R
No tension 520/m	No.3	0.00	$0.1210\sqrt{t}$	0.9991
		1.00	$0.1142\sqrt{t - 170}$	0.9859
		2.00	$0.0886\sqrt{t - 460}$	0.9578

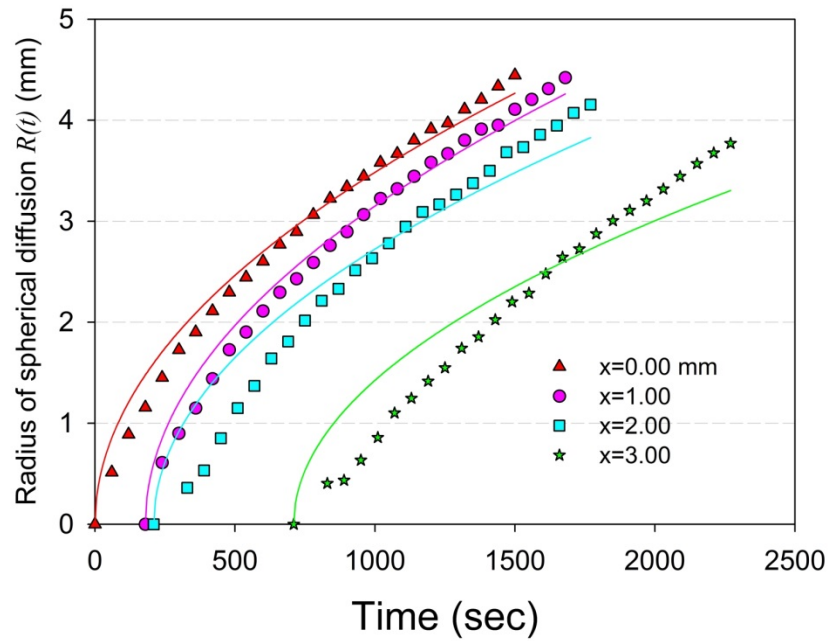


Figure 3.17 Plot of the diffusion radius R against t and x . Sample no.1 with 3N tension and twisting of 520/m

Table 3.11 Regression functions α_x and R value of sample no.1 with 3N tension and twisting of 520/m

Fiber condition	Sample	Measurement point (mm)	Regression curve $R_x(t) = \alpha_x \sqrt{t - t_s}$	R
3N 520/m	No.1	0.00	$0.1102\sqrt{t}$	0.9919
		1.00	$0.1100\sqrt{t - 180}$	0.9926
		2.00	$0.0969\sqrt{t - 210}$	0.9614
		3.00	$0.0836\sqrt{t - 710}$	0.9435

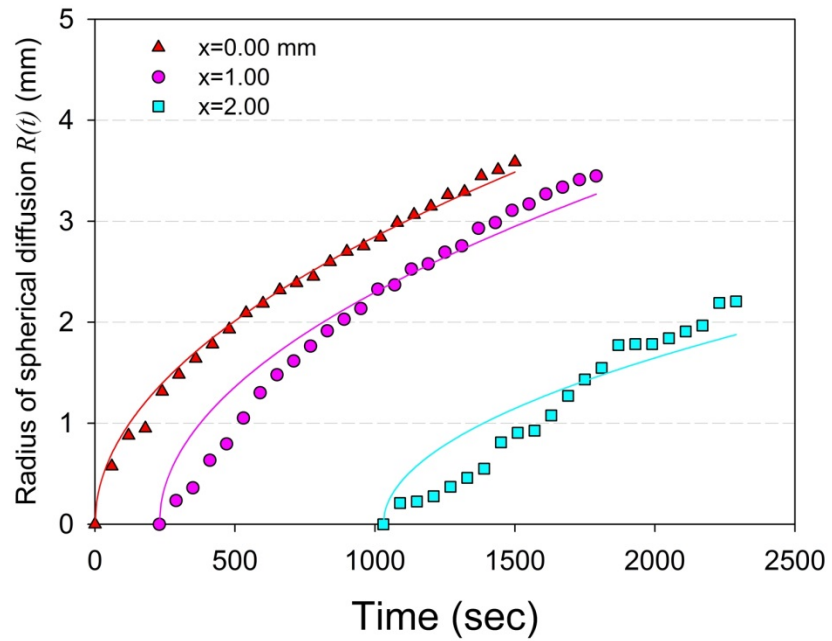


Figure 3.18 Plot of the diffusion radius R against t and x . Sample no.2 with 3N tension and twisting of 520/m

Table 3.12 Regression functions α_x and R value of sample no.2 with 3N tension and twisting of 520/m

Fiber condition	Sample	Measurement point (mm)	Regression curve $R_x(t) = \alpha_x \sqrt{t - t_s}$	R
3N 520/m	No.2	0.00	$0.0900\sqrt{t}$	0.9966
		1.00	$0.0827\sqrt{t - 230}$	0.9729
		2.00	$0.0529\sqrt{t - 1030}$	0.9184

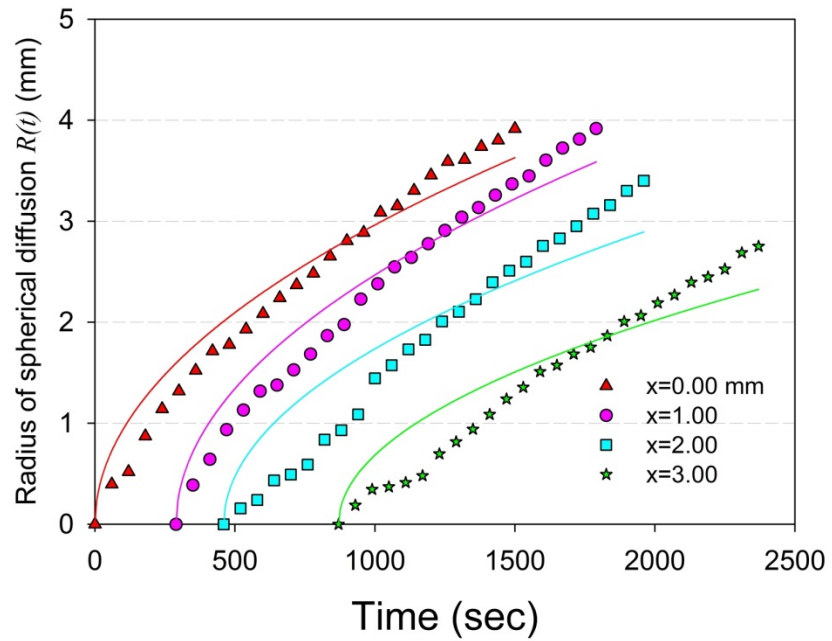


Figure 3.19 Plot of the diffusion radius R against t and x . Sample no.3 with 3N tension and twisting of 520/m

Table 3.13 Regression functions α_x and R value of sample no.3 with 3N tension and twisting of 520/m

Fiber condition	Sample	Measurement point (mm)	Regression curve $R_x(t) = \alpha_x \sqrt{t - t_s}$	R
3N 520/m	No. 3	0.00	$0.0937\sqrt{t}$	0.9773
		1.00	$0.0926\sqrt{t - 290}$	0.9756
		2.00	$0.0747\sqrt{t - 460}$	0.9291
		3.00	$0.0600\sqrt{t - 870}$	0.9335

3.2.3 Computational estimation of diffusion behavior

Equation (6) which explains the diffusion behavior in agarose gel can be constructed as a matrix \bar{R} which is consisted of a augmented matrix of $\bar{L}(t)$ and $\bar{r}(t)$:

$$\bar{R} = [\bar{L}(t) \quad \bar{r}(t)] \quad (7)$$

$$\bar{L}(t) = \begin{bmatrix} L(t_0) \\ L(t_1) \\ L(t_2) \\ \vdots \\ L(t_{n-1}) \end{bmatrix} \quad (8)$$

$$\bar{r}(t) = \alpha_{0,FC} \left[\left(e^{-L(t_{m-1})/\xi_{FC}} \cdot H(t - t_{n-1}) \right)_{m,n} \right] \sqrt{t}$$

$$\text{and elements } \left(e^{-L(t_{m-1})/\xi_{FC}} \cdot H(t - t_{n-1}) \right) = 0 \text{ if } m > n \quad (9)$$

where a subscript *FC* of α and ξ denotes the classification index against geometric variation of fiber such as tension and twisting number per unit length. The (m,n) element of $\bar{r}(t)$ represents the radius of spherical diffusion front from the point $L(t_m)$ when the elapsed time t_n with $m, n = 0, 1, \dots, n-1$. Lower triangular

elements of $\bar{r}(t)$ should be zero by the result of time delay due to capillary speed in Kevlar fiber.

Instead of averaging, regression coefficient $\alpha_{0,FC}$ and ξ_{FC} was calculated from the individual samples above because all of measurement point x are slightly different each other. The distribution plot of coefficient $\alpha_{0,FC}$ against x is shown in figure 3.20.

Using MATLAB, the diffusion behavior in agarose gel is estimated based on the experimental results of $\alpha_{0,FC}$, ξ_{FC} and l_{FC} listed in table 3.14. As mentioned above, $\alpha_{0,FC}$ and l_{FC} were calculated in second and minute scale, respectively. To compensate scale effect, $\alpha_{0,FC}$ in MATLAB code was converted in second scale.

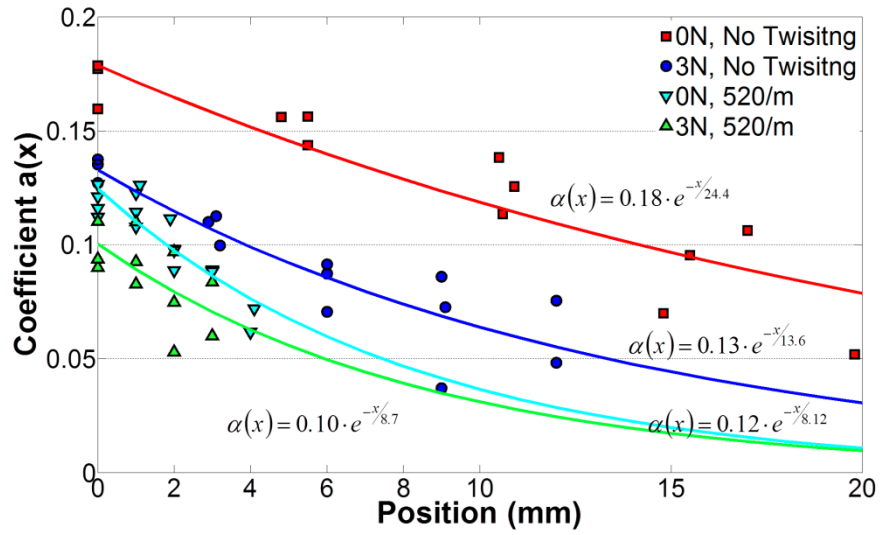


Figure 3.20 Regression plot of coefficient $\alpha_{0,FC}$ and ξ_{FC} against geometrical variation of fiber

Table 3.14 Regression coefficient $\alpha_{0,FC}$, ξ_{FC} and l_{FC}

Geometric variation		$\alpha_{0,FC}$	ξ_{FC}	l_{FC}	Coaxial porosity	Macro image
Tension	Twisting					
0 N	No	0.18	24.4	5.57	60.1 %	
3 N		0.13	13.6	2.66	55.5 %	
0 N	520 /m	0.12	8.12	1.05	51.1 %	
3 N		0.10	8.7	0.69	46.8 %	

Below four figures from 3.21 to 3.24 are the comparison results of the real and estimated diffusion shapes against four different fiber conditions. When a capillary front in fiber touched the wall of agarose gel, the instant was defined as the zero point in time domain.

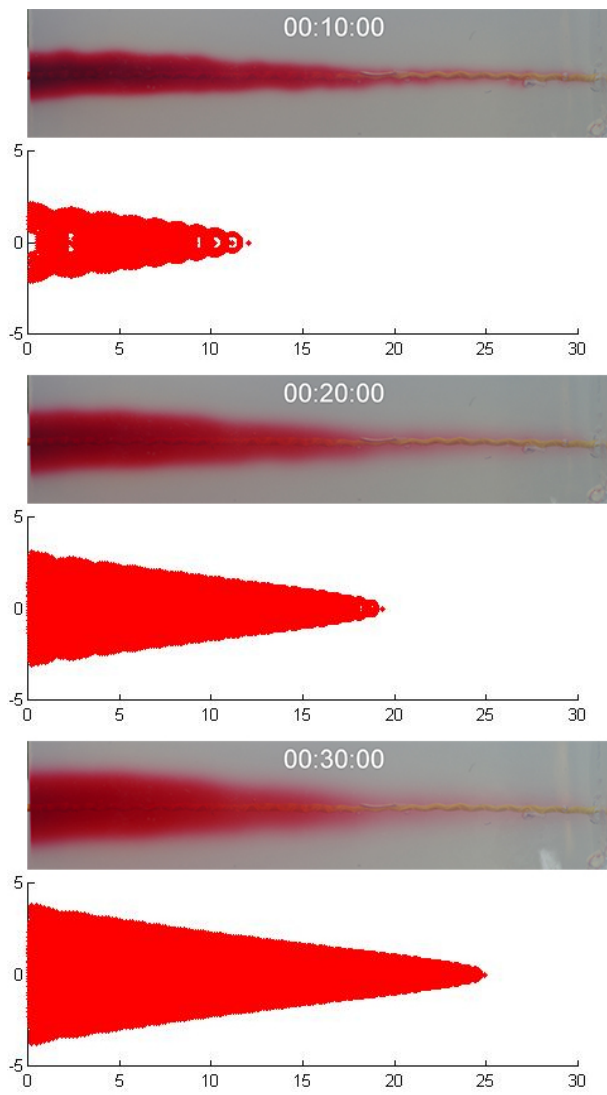


Figure 3.21 Comparison of experimental diffusion behavior in agarose gel and numerical estimation profiles in 10,20,30 min, respectively. No tension and twisting of fiber

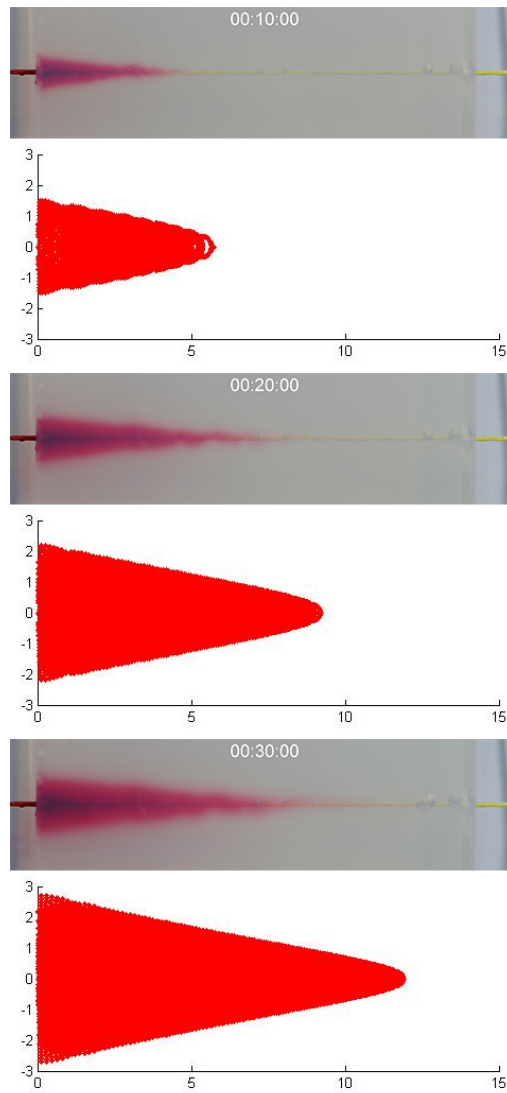


Figure 3.22 Comparison of experimental diffusion behavior in agarose gel and numerical estimation profiles in 10,20,30 min, respectively. 3N tension and no twisting of fiber

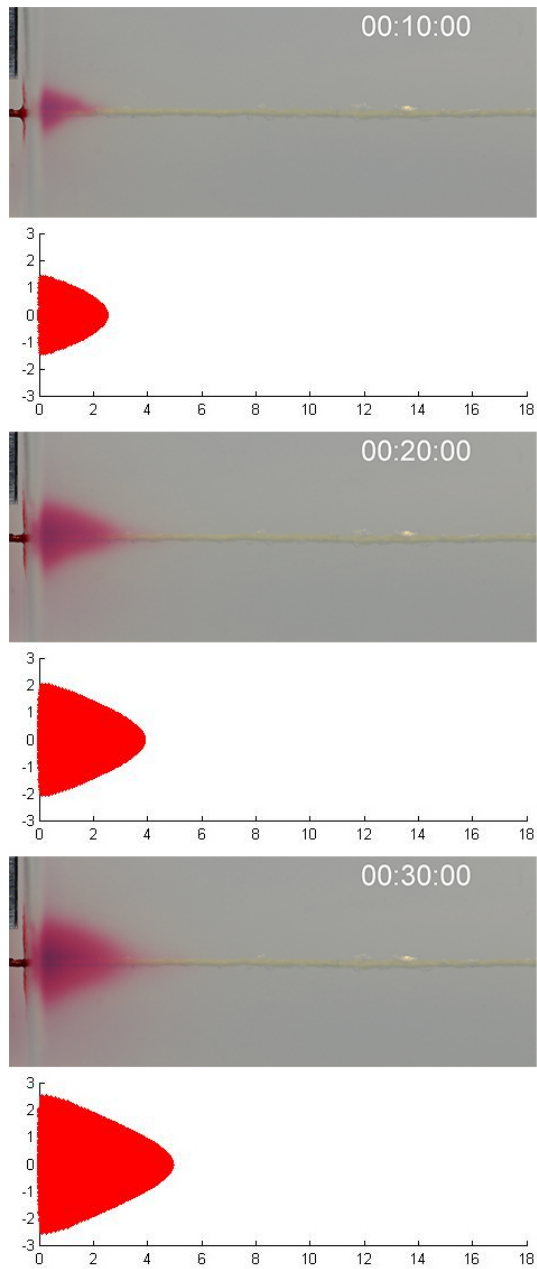


Figure 3.23 Comparison of experimental diffusion behavior in agarose gel and numerical estimation profiles in 10,20,30 min, respectively. No tension and twisting of 520/m

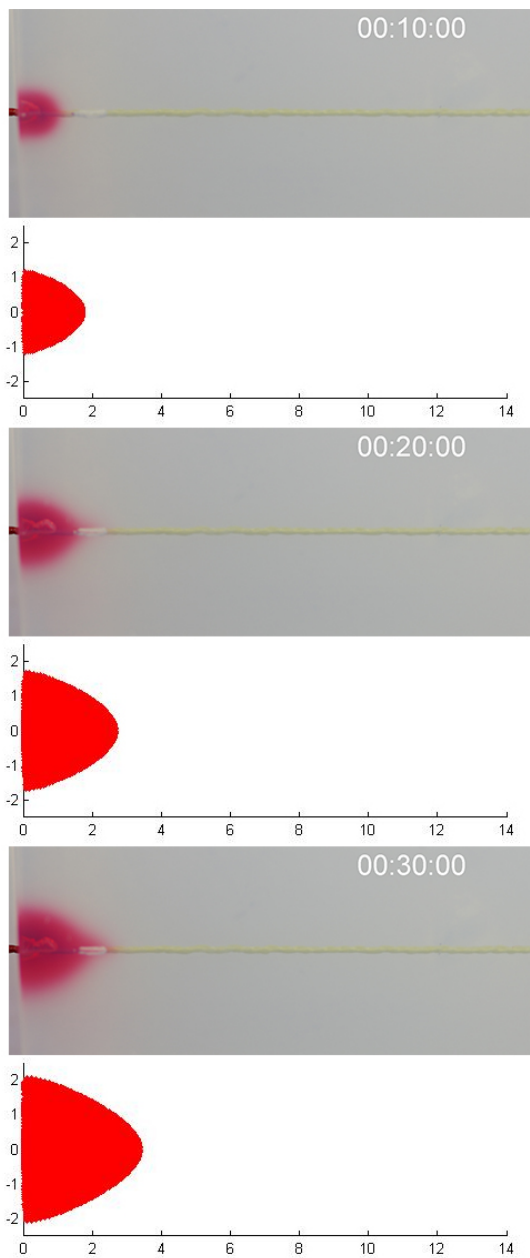


Figure 3.24 Comparison of experimental diffusion behavior in agarose gel and numerical estimation profiles in 10,20,30 min, respectively. 3N tension and twisting of 520/m

3.2.4 Results and discussion

Diffusion and dispersion dynamics in porous media has been studied in a various conditions [54-57]. In agarose gel as a surrogate of brain, the diffusion behavior of liquid via fiber can be assumed as a competitive absorptivity system of agarose gel and fiber inserted. If a surface condition and specification of fiber is fixed, absorptivity of a fiber is physically related to a coaxial porosity which is adjustable by tension and twisting. The graph given in figure 3.25 explains a relation of coaxial porosity and a capillary flow resistance. Black bars in B of figure 3.25 represent capillary inhibition length C and gray bars indicate the absorbed length by agarose gel after 20 min cutting off red dye. In the case of fibers without twisting, absorbed length A are up to 30 mm over the distance of red dye to the intersection, while there is no absorption by agarose gel when fibers are twisted 520 rotates/m. Split ratio τ might be considered as an absorptivity of agarose gel and absorbed length A is supposed to be positively related to τ . In addition, if the capillary inhibition length $L_{\text{gel}}(t_n)$ of fiber in agarose gel does not exceed the capillary inhibition length $L_{\text{air}}(t_n)$ of fiber in air, absorptivity of gel τ ranges from 0.5 to 1 because of $\tau > 1 - \tau$ and $1 - \tau > 0$, definitely.

R/L ratio against t is plotted in figure 3.26. As τ approaches to 0.5, R/L ratio should be decrease and the liquid diffusion shape in agarose gel shows stretched

along fiber. On the contrary, larger τ allows R/L ratio to increase, hence hemispherical shape will appear.

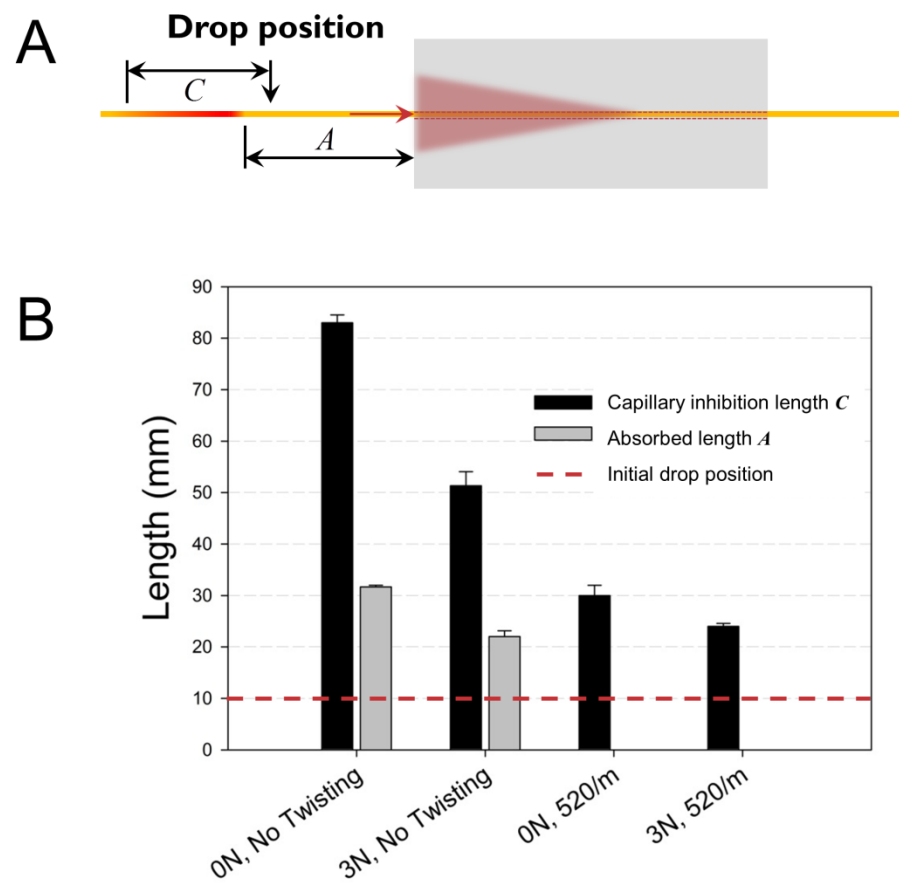


Figure 3.25 Capillary inhibition length C toward opposite side of agarose gel and absorbed length A according to geometric variation of fiber

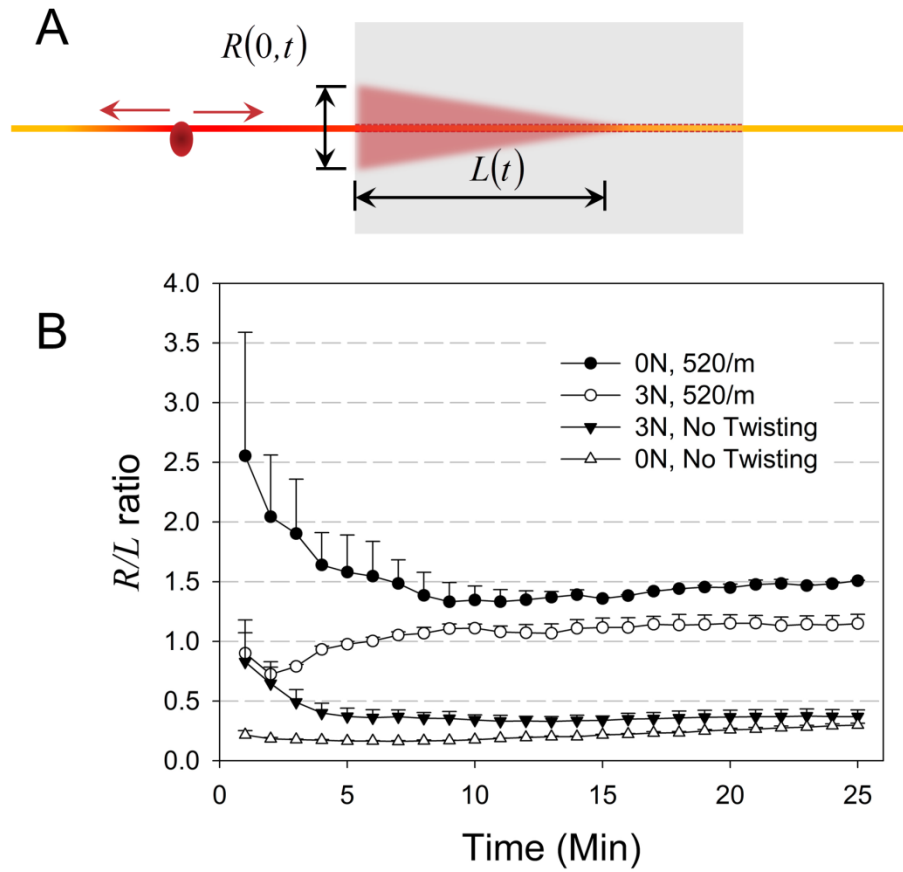


Figure 3.26 Plot of $R_{x=L(0)}(t)/L(t)$ ratio of diffusion profile against time t (min) according to geometric variation of fiber

3.3 Drug delivery via the fiber-embedded channel

3.3.1 Measurement of flow rates

We applied agarose gel as a brain phantom. The range of 0.6 to 1% agarose gel is widely used as a surrogate for in vivo brain because of similarity of infusion-based drug delivery [58, 59]. 2.5 g of Agarose powder (SeaKem LE 50004, Lonza, 50004, USA) was dissolved in 270 ml of distilled water and pH of the solution is adjusted to neutral. The mixture was heated until the agarose powder solution giving transparency. The agarose solution was boiled to eliminate most of bubbles. When the volume of boiling solution reached 250 ml, it was poured into a rectangular mold with a cover to prevent evaporation during gelation. Agarose gels were sectioned as a hexahedron 35 mm on a side.

The experimental setup is shown in Figure 5A. Agarose gel block is immersed in 1X aCSF (Artificial Cerebrospinal fluid), and we inserted the integrated device into the center of gel. The integrated devices were used to characterize a flow rate and the device has two of Kevlar embedded fluidic channels as shown in Figure 1A. However, it is necessary to measure a flow rate via single channel to exclude a crosstalk effect and/or reabsorption that appear at the release ports. One of the fibers was then removed so that single fluidic channel was activated. We used

Rhodamine B (R6626, Sigma, USA) and FITC-BSA (A9771, Sigma, USA) as a high molecular weight protein. Rhodamine can be an alternative molecule because molecular weight of steroid compound ranges from 300 to 500 g/mol. The molar concentrations of 0.1mM and 1mM were used for the dyes, and the dye solution was allowed to supply only one channel of the device. Agarose gel and drug delivery channel were humidified and isolated from air to prevent evaporation of dye solution and agarose gel. Prior to measurement of a flow rate, we confirmed that 10 μ l of water droplet has kept its volume for two days in the experiment setup, hence evaporation loss is negligible. Drug reservoir shown in supplement Figure 2 was connected with the inlet of fiber channel. To exclude an initial fiber wetting time by first dye supply, we set the zero point when the delivery front appears at the release port. In every case, we acquired elapsed time from the zero point and the volume of delivered dye over 12 hours.

Flow rate of two types of dye solution in the integrated device is given in Figure 3.27. In the case of Rhodamine solution, the flow rate shows a positive tendency with molar concentration and the size of gel block. Higher concentration of dye solution increases the mass flux of molecules in the agarose gel, and the larger gel contributes to increase the flow rate. The flow rate of FITC-BSA solution shows similarity to Rhodamine, however overall values are below the half. It can be seen that the concentration of solute at the release region changes slowly due to its high molecular weight.

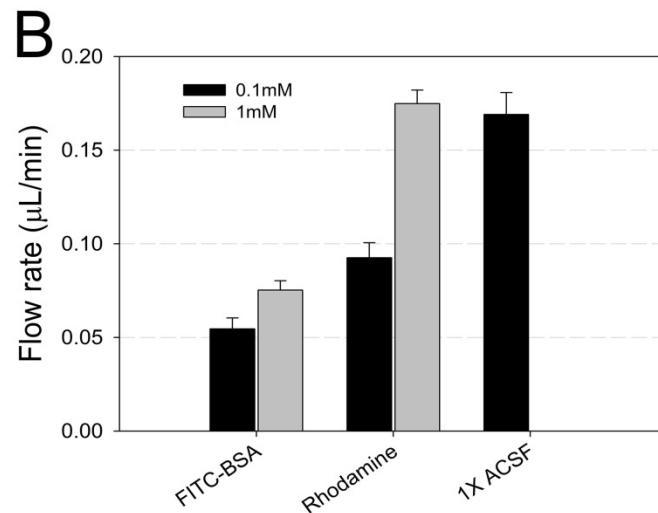
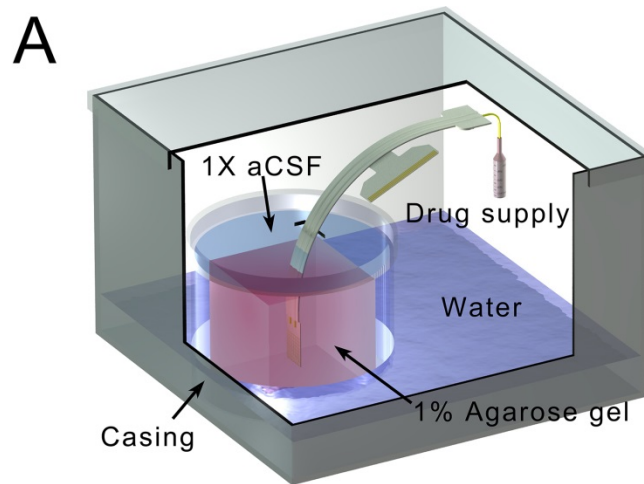


Figure 3.27 Illustration of the experimental setup and the comparison graph of flow rate according to dye and molar concentration. 1X aCSF is control

In addition, we have measured the flow rate of geometric variations of embedded Kevlar fiber. The capillary flow given in figure 3.3 indicates that

capillary flow resistance of fiber is more susceptible to twisting number than induced tension. For obvious difference, three variation of no twisting, 260/m, 520 /m were prepared and there was no tension. We used 1mM Rhodamine solution and the data in figure 3.28 was obtained using 10 samples.

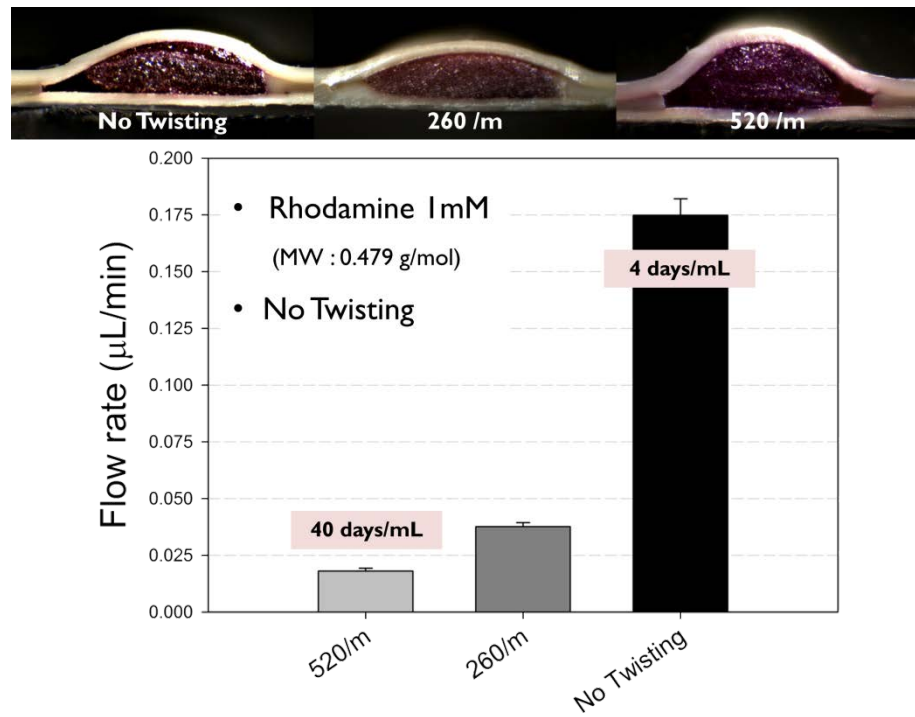


Figure 3.28 The comparison graph of the flow rate according to twisting number of embedded-fiber

There are sectional 10X microscope images of the tested samples over the vertical bar. Because we fabricated mock-up device for the drug delivery experiment, metal interconnections does not appear in sectional images. Inherent color of Rhodamine is clearly shown inside interfilament space. Cross-sectional shape of fiber bundle is deformed during thermal pressure bonding step, however the embedded fiber preserves geometrical property. The flow rate ranges the order of 0.01~0.1 μ L/min and it means 1mL of 1mM Rhodamine can deliver into target tissue for 4~40 days.

3.3.2 Functionality

In aspect of function, figure 3.29 demonstrates a sequential flow of two color water soluble dye via fiber channel. For the obvious visualization, we used red and green water soluble dye. Delivery is allowed to release at the front of channel that is indicated by arrow. Figure 3.29 (a) shows the initial stage of red dye delivery and the first delivery step is observed until (c). After fully releasing of red dye shown in (d) and (e), green dye was added at the inlet of the integrated device.

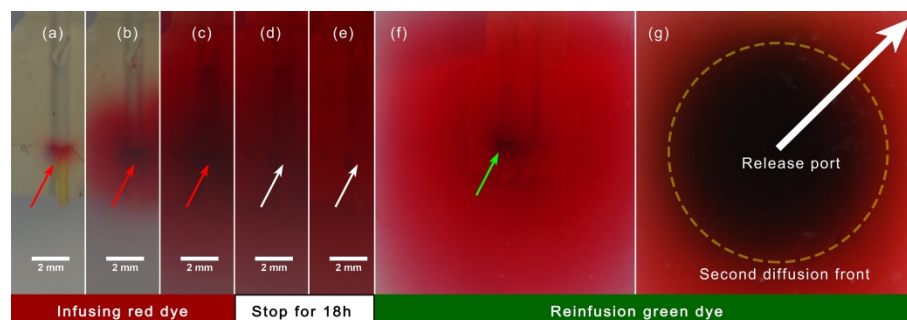


Figure 3.29 Time-lapse images of sequential drug delivery via fiber-embedded channel

Green dye began to be released to an agarose gel again, and additional diffusion of green dye did not influenced by red dye in gel. This result implies two of important advantages of fiber embedded drug delivery mechanism. First,

reabsorption of diffused molecule in target tissue does not occur. 1% agarose gel as a brain phantom has higher absorptivity better than fiber bundle. Therefore, drug delivery proceeds one-way by means of a difference of absorptivity. In addition, reversible flow does not occur because capillary flow is not affected by hydraulic pressure such as brain pressure. Second, drug injection can be scheduled as necessary because discontinuous release of same or different type of drug is possible.

Next is a function of drug delivery toward a contact surface of two agarose gel blocks. Until now, all of experiments have been operated under the condition of implanted channel in agarose gel. However, planar types of neural probes are available for recording and/or stimulus on brain cortex. Electrode opening are located in the comb-like strips at the end of the probe to reduce local bending resistance to enhance contact efficiency of electrodes to the tissue. Since the drug delivery channels terminate immediately before the comb-like strips, the gaps between strips also help drug to diffuse around the probe to the backside of drug release ports. Figure 3.30 demonstrates the time-lapsed images of diffusion profile from a contact surface. Red and green water soluble dyes were delivered and the release ports of channel oriented toward top block. Diffusion beneath the contact surface was caused by backward drug delivery through the interspace between the comb-like strips.



Figure 3.30 Time-lapse images in case of drug delivery toward a contact surface of two 2% agarose gel blocks

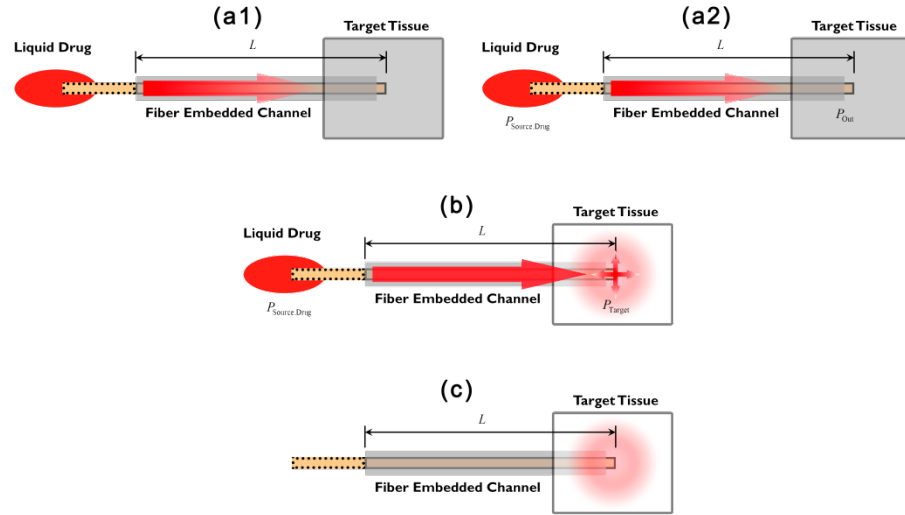


Figure 3.31 Three different stages of drug delivery process

When the fiber-embedded drug delivery system is implanted into a target tissue, drug delivery process can be classified into three stages of (1) drug transport via channel, (2) drug releasing into target and (3) fully released. In the first step of drug transport via channel, drug of liquid phase in source moves and fills the fiber in channel, the illustrations (a1) and (a2) in figure 3.31 indicate this step. When the embedded fiber is dried, the dominant driving force to move drug is a capillary force between liquid drug and solid parts of the system such as filaments of fiber and inner LCP film walls encapsulating fiber. If the fiber is prewetted by water of (a2), fluid flow in fiber can be identified by a Darcy's law which experimentally postulates a difference of pressure as a driving force.

$$Q = -k \frac{A}{\mu} \cdot \frac{\Delta P}{L} \quad (10)$$

where k is the permeability of channel system and μ is the viscosity of drug. Following Darcy's law, flow rate Q via porous channel of length L is proportional to a pressure difference of drug species. Absorbed quantity of drug on Δl of fiber is uniform along fiber, flow speed might be constant against time t because P_{Out} is zero and the same is found in figure 3.2.

Since drug diffusion into target tissue is coupled with overall flow rate, flow kinetics of drug releasing step is more complex. When a drug front in fiber arrives at target tissue, P_{Out} in equation (10) should be denoted as P_{Target} of (b) in figure 3.31. P_{Target} will increase instantly and it increases an overall flow resistance. Furthermore, the negative gradient of pressure from the release port of the device becomes the driving force of diffusion by Fick's second law. As the result, a flow rate during drug releasing step will be determined by physical parameter of drug and porous media such as permeability, viscosity and diffusivity coefficient.

Fully released step means that drug solution in fiber is completely absorbed by target tissue and this step was shown in (e) of figure 3.29 clearly. Agarose gel as a brain phantom is a kind of hydrogel, and water in gel is ensnared by surface tension effect of polymer network. This surface tension is greater than the surface tension between water in gel and fiber, reversible capillary flow does not occur after fully drug released step.

Chapter IV

Drug reservoir module

In this chapter, a novel drug reservoir module compatible with fiber embedded drug delivery channel is described. As mentioned, conventional microfluidics including drug delivery micro-channel needs an auxiliary pump to flow liquid in channel. To prevent pressure loss and/or leakage, tight fitting joint connecting channel, pump and drug reservoir is essential part.

Fiber-embedded drug delivery channel operates without help of pump, while fiber at the inlet side should be immersed in drug chamber. Tight fitting joint for our system is also necessary, although drug delivery in fiber is based on capillary flow. For the approach this problem, we have to consider a representative characteristic of capillary flow in fiber, i.e., sheath flow around fiber. Therefore we have to develop a novel fitting joint mechanism because fiber-embedded drug delivery channel is the first report in this research field. Development and design constraints are defined like below

- (1) Compatibility with multi-channel system
- (2) Portability and integrated system

- (3) Refillable and expandable drug chamber
- (4) No exposure to air. (Anti-evaporation of drug, anti-contamination)
- (5) Shock and vibration resistance

The integrated device has two of drug delivery channels and the width of single channel is below 1.3 mm. One of the advantages of our approach is expandability of channel number. Number of embedded channel is important because it is necessary to supply one or more drugs into target tissues. That is the reason drug reservoir should be compatible with multi-channel system. In addition, refilling function has to be possible for a continuous and long-term implantation. To prevent contamination by aerobic bacteria and etc., inlet part of fiber should be isolated with air.

4.1 Sealing mechanism

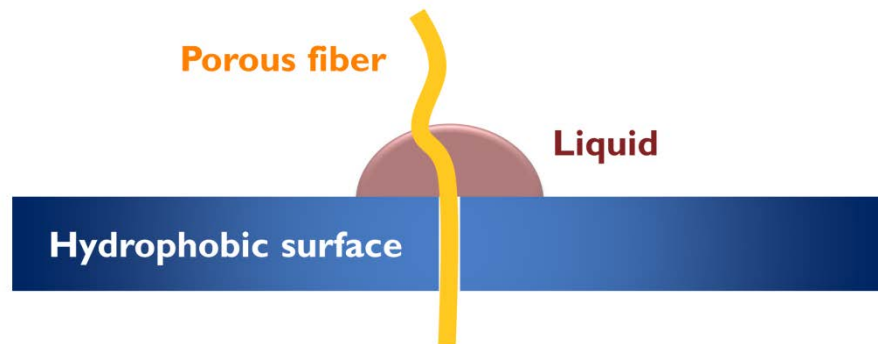


Figure 4.1 Illustration of sealing idea using a hydrophobic barrier

The illustration given in figure 4.1 represents a conceptual isolation mechanism of bulk flow of liquid. When a porous fiber is penetrated an isolation barrier with hydrophobic surface, liquid on one side can only transfer via a porous fiber without leakage through the gap because of low surface energy density at the liquid-surface interface. For the validation above idea, a simple test was performed shown in figure 4.2. We penetrated a Kevlar fiber through PDMS block with 2 mm thickness. And 100 μl of red water soluble dye was dropped on upper surface. Time-lapse images with 10 seconds interval are shown in figure 4.2. We confirmed that the result follows the sealing idea demonstrated above.

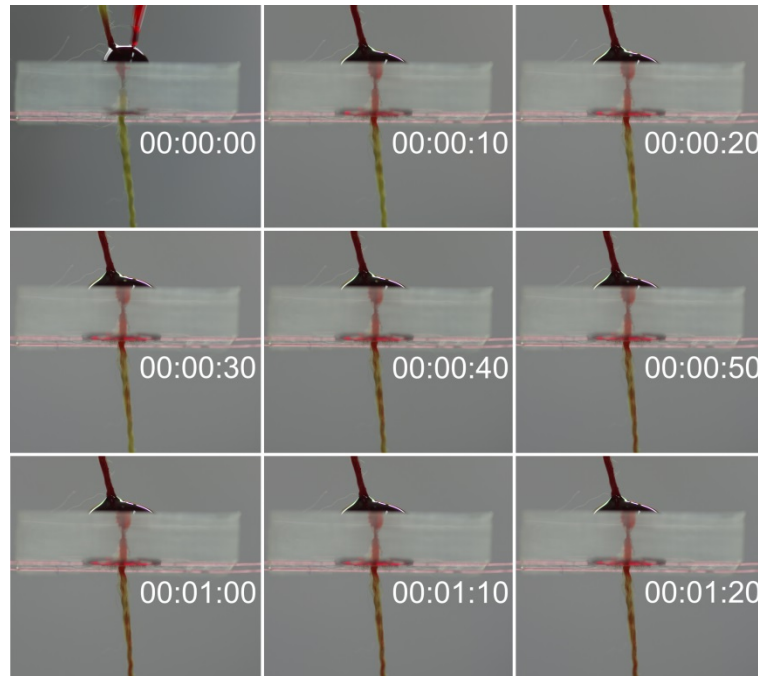


Figure 4.2 Time-lapse images of capillary flow in Kevlar fiber penetrated PDMS barrier

4.2 Design and assembling

Figure 4.3 is a sectional 3D rendering model of drug reservoir module which agrees the design constrains. This module is composed of two drug chambers and fiber distributor which serves as a chamber connector. Each drug chamber has a cap, so drug can be refilled and replaced if necessary. Enlarged illustration in dash line

box shows the detailed structure. The bottom of each drug chamber is coated 2 mm thickness Polydimethylsiloxane (PDMS) as a hydrophobic barrier, and each fiber at the inlet side is connected to the inside of chamber. Fiber distributor of black colored in figure 4.3 plays an important role. First, this part broadens a gap between two fibers not to contact each other. Second, distributor insulates fibers against air for the purpose of evaporation suppression and prevention of contamination by aerobic bacteria and microbes.

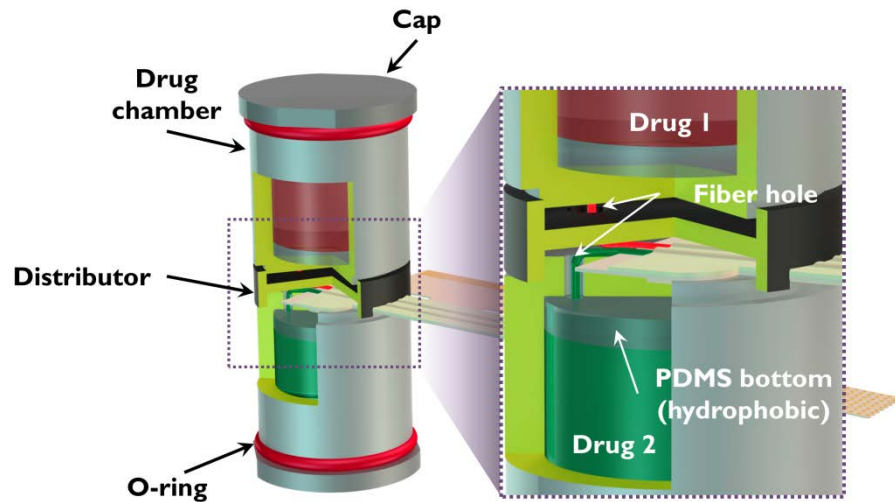


Figure 4.3 Rendering image of the drug reservoir module compatible with the 64 ch. integrated device

The photographs of the prototype are shown in figure 4.4. Fiber hole of 1mm diameter is drilled on each drug chamber, and each fiber is inserted through the hole, individually.

A



B



Figure 4.4 The prototype of drug reservoir module. **A.** Photographs of parts. **B.** Assembled image

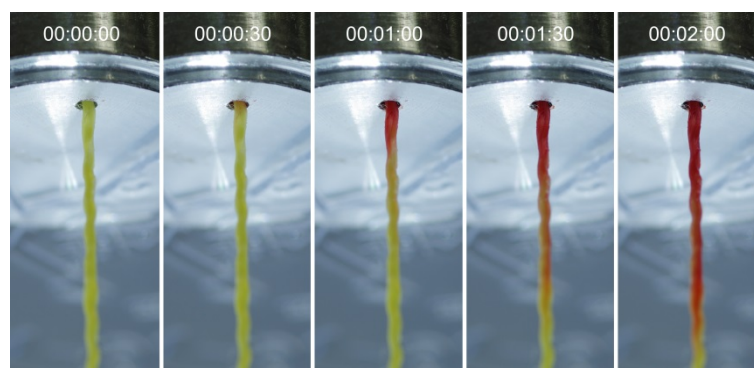


Figure 4.5 Time-lapse images of capillary flow in Kevlar fiber penetrated PDMS coated drug chamber

In figure 4.5, sealing performance of the PDMS coated drug chamber. The same with figure 4.2 was founded and leakage via fiber hole never appeared.

4.3 Limitation and future work

The prototype of drug reservoir was machined using aluminum alloy 6061 series. For a clinical application, it is necessary to apply a disposable material for a mass production and low cost. Cyclic olefin copolymer (COC) might be an excellent alternative material for the purpose in terms of productivity and economic feasibility. One of the problems associated with hydrophobicity can be solved by surface treatment technique including Teflon coating.

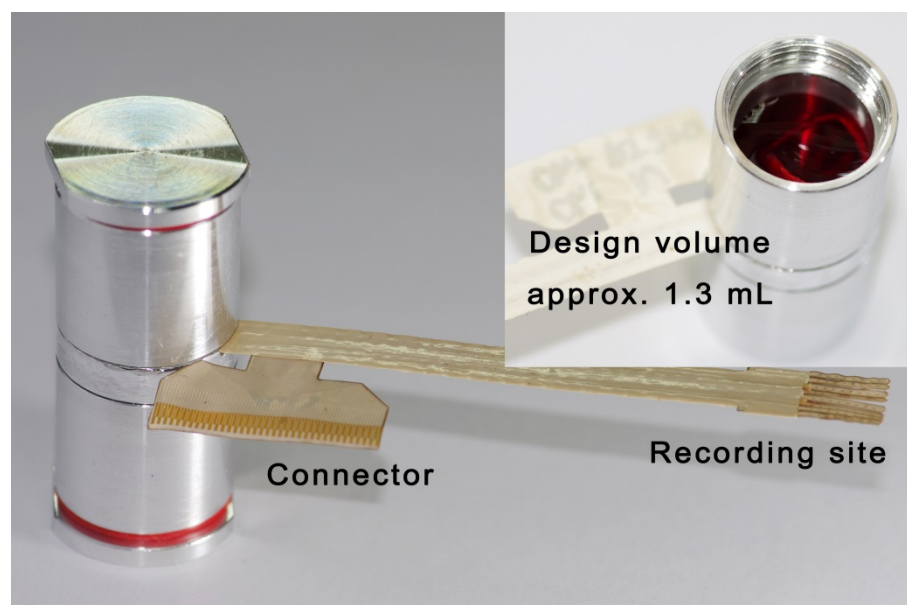


Figure 4.6 Photograph of final assembled system including 64 ch

In addition, we found that the tapped cap causes a liquid pressurization which pushes liquid out through the fiber hallway shown in figure 4.3. Needle injection type can be an alternative, because air in an empty drug chamber releases through the fiber holes by filled liquid drug. In a view point of practical application, injection method is safe better than a tapped cap type.

Chapter V

Conclusion

A novel pumpless drug delivery channel for flexible neural probe was designed and fabricated using LCP films as encapsulation and metallization substrates. Monolithic integration of electrodes with fluidic channels was achieved by thermal bonding process that exploited directional heating to selectively melt and bond MEA patterned with guide, cover LCP films. The fluidic channels are formed by placing Kevlar fibers between the LCP films during bonding process. Integration process of the fiber embedded channel is significantly simpler to fabricate when compared to conventional etched microchannels fabricated by micromachining.

Cyclic voltammetry and impedance spectroscopy were measured and the electrodes and dense metal interconnections were functional and retained original electrical impedance. In terms of fluidic channel, the kinetics of capillary flow in Kevlar fiber was studied; dry Kevlar fiber follows Washburn's law, while the liquid length h of pre-wetted Kevlar fiber is farther two times over than dry one and the curve as a function of time is linear.

Table 5.1 Comparison list of fiber-embedded drug delivery channel system and conventional system

	Fiber-embedded drug delivery channel	Conventional drug delivery channel
Cost	Extremely low	High
Productivity	Compatible with mass production	Not available
Mechanical reliability	Excellent	Weak to external force
Biocompatibility	Available	Available
Flow rate	Controllable by geometric variation of fiber	Controllable by external pumps
Dimension scale	Less than mm scale	Less than μm scale
Drug refilling	Possible	Partially impossible
Integration	Individual add-on is possible	Built-in type

This is an important cue to extend capillary length in fiber; our devices are allowed to proceed under pre-wetted condition.

A porous fiber and a brain can absorb a liquid, either. Fortunately, absorptivity of a brain is higher than a porous fiber; hence drug moving

direction orients toward a brain. Liquid transport and diffusion in a target tissue can be modeled as absorptivity (of fiber)-an absorptivity (of target tissue) competitive system. By means of several assumptions, diffusion behavior in a brain phantom (1% agarose gel) has been successfully analyzed. In this result, split ratio τ (similar to relative absorptivity physically) was introduced and it is confirmed that τ can be adjusted by geometric variation of fiber.



Figure 5.1 Rendering image of the flexible LCP film-based neural probe with the fiber-embedded drug delivery channels

Drug reservoir compatible with fiber-embedded channel system has been developed successfully. Consequently, an innovative whole system was introduced in this thesis. Representative specifications of the system are compared with a conventional drug delivery system, and the chart is listed in

table 5.1. In comparison with conventional system, pumpless drug delivery system has several advantages.

(1) Liquid drug can be infused without helps of auxiliary pumps.

Fiber-embedded drug delivery system is based on a capillary action in porous fibers. Pressure driven flow into a brain might be harmful on local brain tissue because brain pressure can increase by means of the driving pressure. On the other hand, a driving force of drug depends on a balance between an absorptivity of porous fiber and target when our system is implanted a target tissue. An embedded fiber serves as a pipeline after implantation. Therefore, there is no increment of local brain pressure and tissue reaction can be minimized by pressure.

(2) Low cost and mass productivity

Neural prosthesis with drug delivery channel is a promising alternative for patients with nervous system diseases. Although an excellent treatment efficacy, commercialization of conventional researches is not available due to fabrication complexity and high cost for manufacturing.

A fiber embedded drug delivery system can be easily fabricated by a simple thermal pressure lamination method with low cost, and production yields can be improved by means of scale up of mold.

(3) Mechanical reliability and durability

In terms of mechanical property, conventional microfluidic based drug delivery channels are vulnerable to a physical deformation and external force. Etched and micro-machined hollow structure is advantageous in a view point of micro-scale device, whereas mechanical durability of those can cause critical issues in long-term implantation of system.

Major advantage of the fiber embedded drug delivery system is high mechanical reliability and durability. In a view point of architecture, fibers filled inside channel serve as a supporting structure which prevents clogging and collapsing by bending and folding. Moreover, fiber prevents a clogging by tissue debris during insertion step.

However, the dimensional scale of our approach needs to be minimized. The key factor that defines a scale is a diameter of fiber. Kevlar fiber applied in this dissertation is consisted of 800 filaments with a diameter of 10 μm . It was not possible to manipulate the dimension of fiber; hence there was a limitation to adjust the dimension of final product including geometric variations. If a thinner fiber is applied, dimensional feature of a fiber embedded drug delivery system can be minimized below micro scale and more complex characteristics of flow rate can be mapped.

Our approach is the first report in the field of drug delivery systems on neural probes; the mechanical and functional concept can be one of the original technologies in neural prosthesis market. For the commercialization, some aspects of this system should be evaluated and improved including the scale-

down problem. To verify the overall performance, long-term in-vivo experiments are necessary. Dynamics and controllability of drug infusing should be assessed by animal experiments, and we have to analysis reactions of animals to drug infusing strategies. In addition, an integration density of drug delivery channel can be enhanced to meet the clinical characteristics.

Throughout continued technical developments and innovations, we hope that this simple fabrication combined with robust performance characteristics of fiber-embedded drug delivery approach has potential for applications in a number of implantable medical devices such as neural prosthesis.

Bibliography

- [1] Cheung, K.C., *Implantable microscale neural interfaces*. Biomedical Microdevices, 2007. **9**(6): p. 923-938.
- [2] Wise, K.D., J.B. Angell, and A. Starr, *An integrated-circuit approach to extracellular microelectrodes*. IEEE Trans Biomed Eng, 1970. **17**(3): p. 238-247.
- [3] Wise, K.D. and J.B. Angell, *A low-capacitance multielectrode probe for use in extracellular neurophysiology*. IEEE Trans Biomed Eng, 1975. **22**(3): p. 212-219.
- [4] Campbell, P.K., K.E. Jones, R.J. Huber, K.W. Horch, and R.A. Normann, *A silicon-based, three-dimensional neural interface: manufacturing processes for an intracortical electrode array*. IEEE Trans Biomed Eng, 1991. **38**(8): p. 758-768.
- [5] Kuo, J.T.W., B.J. Kim, S.A. Hara, C.D. Lee, C.A. Gutierrez, T.Q. Hoang, and E. Meng, *Novel flexible Parylene neural probe with 3D sheath structure for enhancing tissue integration*. Lab on a Chip, 2013. **13**(4): p. 554-561.
- [6] Takeuchi, S., D. Ziegler, Y. Yoshida, K. Mabuchi, and T. Suzuki, *Parylene flexible neural probes integrated with microfluidic channels*. Lab Chip, 2005. **5**(5): p. 519-523.
- [7] Mercanzini, A., K. Cheung, D.L. Buhl, M. Boers, A. Maillard, P. Colin, J.C. Bensadoun, A. Bertsch, and P. Renaud, *Demonstration of cortical recording*

- using novel flexible polymer neural probes*. Sensors and Actuators a-Physical, 2008. **143**(1): p. 90-96.
- [8] Metz, S., A. Bertsch, D. Bertrand, and P. Renaud, *Flexible polyimide probes with microelectrodes and embedded microfluidic channels for simultaneous drug delivery and multi-channel monitoring of bioelectric activity*. Biosensors & Bioelectronics, 2004. **19**(10): p. 1309-1318.
- [9] Takeuchi, S., T. Suzuki, K. Mabuchi, and H. Fujita, *3D flexible multichannel neural probe array*. Journal of Micromechanics and Microengineering, 2004. **14**(1): p. 104-107.
- [10] Myllymaa, S., K. Myllymaa, H. Korhonen, J. Toyras, J.E. Jaaskelainen, K. Djupsund, H. Tanila, and R. Lappalainen, *Fabrication and testing of polyimide-based microelectrode arrays for cortical mapping of evoked potentials*. Biosens Bioelectron, 2009. **24**(10): p. 3067-3072.
- [11] Lago, N., K. Yoshida, K.P. Koch, and X. Navarro, *Assessment of biocompatibility of chronically implanted polyimide and platinum intrafascicular electrodes*. IEEE Transactions on Biomedical Engineering, 2007. **54**(2): p. 281-290.
- [12] Cheung, K.C., P. Renaud, H. Tanila, and K. Djupsund, *Flexible polyimide microelectrode array for in vivo recordings and current source density analysis*. Biosensors & Bioelectronics, 2007. **22**(8): p. 1783-1790.
- [13] Hwang, G.T., D. Im, S.E. Lee, J. Lee, M. Koo, S.Y. Park, S. Kim, K. Yang, S.J. Kim, K. Lee, and K.J. Lee, *In Vivo Silicon-Based Flexible Radio*

- Frequency Integrated Circuits Monolithically Encapsulated with Biocompatible Liquid Crystal Polymers*. *Acs Nano*, 2013. **7**(5): p. 4545-4553.
- [14] Jeong, J., S.W. Lee, K.S. Min, S. Shin, S.B. Jun, and S.J. Kim, *Liquid Crystal Polymer (LCP), an Attractive Substrate for Retinal Implant*. *Sensors and Materials*, 2012. **24**(4): p. 189-203.
- [15] Lee, S.E., S.B. Jun, H.J. Lee, J. Kim, S.W. Lee, C. Im, H.C. Shin, J.W. Chang, and S.J. Kim, *A Flexible Depth Probe Using Liquid Crystal Polymer*. *IEEE Transactions on Biomedical Engineering*, 2012. **59**(7): p. 2085-2094.
- [16] Lee, S.W., K.S. Min, J. Jeong, J. Kim, and S.J. Kim, *Monolithic Encapsulation of Implantable Neuroprosthetic Devices Using Liquid Crystal Polymers*. *IEEE Transactions on Biomedical Engineering*, 2011. **58**(8).
- [17] Lee, S.W., J.M. Seo, S. Ha, E.T. Kim, H. Chung, and S.J. Kim, *Development of microelectrode arrays for artificial retinal implants using liquid crystal polymers*. *Invest Ophthalmol Vis Sci*, 2009. **50**(12): p. 5859-5866.
- [18] Kyou Sik Min, S.E.L., Jung Hun Chang, Ho Sun Lee, Seung Ha Oh, and Sung June Kim, *Development of a Multichannel Cochlear Electrode Arrays using Flexible Liquid Crystal Polymer Films*, in *Flextech 2011/2011*: Arizona Grand Resort, Phoenix, AZ, US.
- [19] Sung Eun Lee, S.W.L., Jin Hyung Kim, Choong Jae Lee, Se-ik, Park, Jin Woo Chang, and Sung June Kim, *Liquid Crystal Polymer based Animal Deep Brain Stimulation Electrode*, in *International Neuromodulation Society 9th World Congress 2009*: Seoul, South Korea.

- [20] Biran, R., D.C. Martin, and P.A. Tresco, *Neuronal cell loss accompanies the brain tissue response to chronically implanted silicon microelectrode arrays*. *Exp Neurol*, 2005. **195**(1): p. 115-126.
- [21] Johnson, M.D., K.J. Otto, and D.R. Kipke, *Repeated voltage biasing improves unit recordings by reducing resistive tissue impedances*. *IEEE Trans Neural Syst Rehabil Eng*, 2005. **13**(2): p. 160-165.
- [22] Kim, D.H. and D.C. Martin, *Sustained release of dexamethasone from hydrophilic matrices using PLGA nanoparticles for neural drug delivery*. *Biomaterials*, 2006. **27**(15): p. 3031-3037.
- [23] Ludwig, K.A., J.D. Uram, J. Yang, D.C. Martin, and D.R. Kipke, *Chronic neural recordings using silicon microelectrode arrays electrochemically deposited with a poly(3,4-ethylenedioxythiophene) (PEDOT) film*. *J Neural Eng*, 2006. **3**(1): p. 59-70.
- [24] Maynard, E.M., E. Fernandez, and R.A. Normann, *A technique to prevent dural adhesions to chronically implanted microelectrode arrays*. *J Neurosci Methods*, 2000. **97**(2): p. 93-101.
- [25] Shain, W., L. Spataro, J. Dilgen, K. Haverstick, S. Retterer, M. Isaacson, M. Saltzman, and J.N. Turner, *Controlling cellular reactive responses around neural prosthetic devices using peripheral and local intervention strategies*. *IEEE Trans Neural Syst Rehabil Eng*, 2003. **11**(2): p. 186-188.
- [26] Szarowski, D.H., M.D. Andersen, S. Retterer, A.J. Spence, M. Isaacson, H.G. Craighead, J.N. Turner, and W. Shain, *Brain responses to micro-machined*

- silicon devices*. Brain Res, 2003. **983**(1-2): p. 23-35.
- [27] Zhong, Y. and R.V. Bellamkonda, *Controlled release of anti-inflammatory agent alpha-MSH from neural implants*. J Control Release, 2005. **106**(3): p. 309-318.
- [28] Bearinger, J.P., S. Terrettaz, R. Michel, N. Tirelli, H. Vogel, M. Textor, and J.A. Hubbell, *Chemisorbed poly(propylene sulphide)-based copolymers resist biomolecular interactions*. Nat Mater, 2003. **2**(4): p. 259-264.
- [29] Heuberger, M., T. Drobek, and N.D. Spencer, *Interaction forces and morphology of a protein-resistant poly(ethylene glycol) layer*. Biophys J, 2005. **88**(1): p. 495-504.
- [30] He, W. and R.V. Bellamkonda, *Nanoscale neuro-integrative coatings for neural implants*. Biomaterials, 2005. **26**(16): p. 2983-2990.
- [31] Marrese, C.A., O. Miyawaki, and L.B. Wingard, Jr., *Simultaneous electrochemical determination of diffusion and partition coefficients of potassium ferrocyanide for albumin-glutaraldehyde membranes*. Anal Chem, 1987. **59**(2): p. 248-252.
- [32] Moxon, K.A., N.M. Kalkhoran, M. Markert, M.A. Sambito, J.L. McKenzie, and J.T. Webster, *Nanostructured surface modification of ceramic-based microelectrodes to enhance biocompatibility for a direct brain-machine interface*. IEEE Trans Biomed Eng, 2004. **51**(6): p. 881-889.
- [33] Mond, H.G. and D. Grenz, *Implantable transvenous pacing leads: the shape of things to come*. Pacing Clin Electrophysiol, 2004. **27**(6 Pt 2): p. 887-893.

- [34] Mond, H.G. and K.B. Stokes, *The electrode-tissue interface: the revolutionary role of steroid elution*. Pacing Clin Electrophysiol, 1992. **15**(1): p. 95-107.
- [35] Spataro, L., J. Dilgen, S. Retterer, A.J. Spence, M. Isaacson, J.N. Turner, and W. Shain, *Dexamethasone treatment reduces astroglia responses to inserted neuroprosthetic devices in rat neocortex*. Exp Neurol, 2005. **194**(2): p. 289-300.
- [36] Ziegler, D., T. Suzuki, and S. Takeuchi, *Fabrication of flexible neural probes with built-in microfluidic channels by thermal bonding of Parylene*. Journal of Microelectromechanical Systems, 2006. **15**(6): p. 1477-1482.
- [37] Wang, X.F., J. Engel, and C. Liu, *Liquid crystal polymer (LCP) for MEMS: processes and applications*. Journal of Micromechanics and Microengineering, 2003. **13**(5): p. 628-633.
- [38] Jeong, J., S.W. Lee, K.S. Min, and S.J. Kim, *A novel multilayered planar coil based on biocompatible liquid crystal polymer for chronic implantation*. Sensors and Actuators a-Physical, 2013. **197**: p. 38-46.
- [39] Henderson, J.D., R.H. Mullarky, and D.E. Ryan, *Tissue Biocompatibility of Kevlar Aramid Fibers and Polymethylmethacrylate, Composites in Rabbits*. Journal of Biomedical Materials Research, 1987. **21**(1): p. 59-64.
- [40] Cogan, S.F., *Neural stimulation and recording electrodes*. Annu Rev Biomed Eng, 2008. **10**: p. 275-309.
- [41] Washburn, E.W., *The dynamics of capillary flow*. Physical Review, 1921.

- 17**(3): p. 273-283.
- [42] Liu, T., K.F. Choi, and Y. Li, *Wicking in twisted yarns*. J Colloid Interface Sci, 2008. **318**(1): p. 134-139.
- [43] Princen, H.M., *Capillary Phenomena in Assemblies of Parallel Cylinders .2. Capillary Rise in Systems with More Than 2 Cylinders*. Journal of Colloid and Interface Science, 1969. **30**(3): p. 359-371.
- [44] Princen, H.M., *Capillary Phenomena in Vertical and Horizontal Assemblies of Parallel Cylinders*. Abstracts of Papers of the American Chemical Society, 1969(Sep): p. Co 42.
- [45] Princen, H.M., *Capillary Phenomena in Assemblies of Parallel Cylinders .3. Liquid Columns between Horizontal Parallel Cylinders*. Journal of Colloid and Interface Science, 1970. **34**(2): p. 171-184.
- [46] Beck, J. and J. Bardeche, [*A new medium with an agarose base for the determination of antibiotics by diffusion methods*]. Ann Biol Clin (Paris), 1965. **23**(7): p. 987-991.
- [47] Davies, P.A., *Determination of diffusion coefficients of proteins in beaded agarose by gel filtration*. J Chromatogr, 1989. **483**: p. 221-937.
- [48] Lead, J.R., K. Starchev, and K.J. Wilkinson, *Diffusion coefficients of humic substances in agarose gel and in water*. Environ Sci Technol, 2003. **37**(3): p. 482-487.
- [49] Nicholson, C., *Diffusion and related transport mechanisms in brain tissue*. Reports on Progress in Physics, 2001. **64**(7): p. 815-884.

- [50] Pun, T., *A New Method for Grey-Level Picture Thresholding Using the Entropy of the Histogram*. Signal Processing, 1980. **2**(3): p. 223-237.
- [51] Sjoberg, H., S. Persson, and N. Caram-Lelham, *How interactions between drugs and agarose-carrageenan hydrogels influence the simultaneous transport of drugs*. Journal of Controlled Release, 1999. **59**(3): p. 391-400.
- [52] Fatin-Rouge, N., K. Starchev, and J. Buffle, *Size effects on diffusion processes within agarose gels*. Biophys J, 2004. **86**(5): p. 2710-2719.
- [53] Pluen, A., P.A. Netti, R.K. Jain, and D.A. Berk, *Diffusion of macromolecules in agarose gels: comparison of linear and globular configurations*. Biophys J, 1999. **77**(1): p. 542-552.
- [54] Fargue, D., P. Jamet, and P. Costeseque, *Dispersion phenomena in thermal diffusion and modelling of thermogravitational experiments in porous media*. Transport in Porous Media, 1998. **30**(3): p. 323-344.
- [55] Valdes-Parada, F.J., C.G. Aguilar-Madera, and J. Alvarez-Ramirez, *On diffusion, dispersion and reaction in porous media*. Chemical Engineering Science, 2011. **66**(10): p. 2177-2190.
- [56] Whitaker, S., *Diffusion and Dispersion in Porous Media*. Aiche Journal, 1967. **13**(3): p. 420-427.
- [57] Yu, D., K. Jackson, and T.C. Harmon, *Dispersion and diffusion in porous media under supercritical conditions*. Chemical Engineering Science, 1999. **54**(3): p. 357-367.
- [58] Chen, Z.J., W.C. Broaddus, R.R. Viswanathan, R. Raghavan, and G.T. Gillies,

Intraparenchymal drug delivery via positive-pressure infusion: experimental and modeling studies of poroelasticity in brain phantom gels. IEEE Trans Biomed Eng, 2002. **49**(2): p. 85-96.

- [59] Chen, Z.J., G.T. Gillies, W.C. Broaddus, S.S. Prabhu, H. Fillmore, R.M. Mitchell, F.D. Corwin, and P.P. Fatouros, *A realistic brain tissue phantom for intraparenchymal infusion studies.* J Neurosurg, 2004. **101**(2): p. 314-22.

초 록

이식형 보철기구를 위한 섬유 기반의 자력 이송 플렉서블 약물 전달 시스템

신경계 질병 치료는 내복약제를 이용한 약물 치료에 한계가 있으므로 인해, 최근 다채널 미세 전극 기반의 이식형 신경 보철을 이용한 직접적인 신경 자극 치료방법이 시도되고 있다. 신경 보철의 장기 이식 과정 이물 반응(foreign body reaction) 및 생체 내 거부반응 (tissue reaction)등의 위험성이 있으며, 이를 억제하기 위한 다양한 형태의 연구가 진행되어 오고 있다. 본 논문은 장기 이식형 신경 보철(chronic implantable neural prosthesis)에 범용적으로 탑재 가능한 미세 약물 전달 채널 시스템의 설계, 제조 및 성능 평가와 아울러 조직 내 약물 확산의 동적 거동에 대한 실험적 분석 결과를 포괄적으로 기술하고 있다. 기존 약물 전달 채널 시스템과의 대표적인 차별성으로 본 연구는 펌프 없이 약물 전달이 가능한 시스템, 초박형 LCP (liquid crystal polymer) 필름 기반의 뇌신경전극과의 일체화, 삽입 시 생체 조직의 상해를 최소화하기 위한 유연성 (flexibility), 낮은 제조 단가 및 높은 생산성 확보를 통해 상업화 가능성을 높인 제조 기술 등을 제시하였다. 아울러 본 논문은 (1)약물 채널 일체성형 기술 구현을 위한 설계, 제조, 해석 결과 (2) 약물 전달 성능 및 특성 분석 (3) 섬유 채널에 특화된 약물 저장/공급부 설계 등 세 부분으로 구성되어 있다.

약물 전달 채널과 LCP 기반의 신경 전극의 일체 성형 기술은 전극의 물

리적 손상 없는 단일화 접합(monolithic bonding) 공정 기술 개발을 목표로 한다. 약물 전달 채널은 정렬층(Guidance LCP layer), Kevlar 섬유, 그리고 포장층(Covering LCP layer)으로 구성되어 있으며, 정렬층의 선택적 상변화를 유도하기 위한 비대칭 가열 접합 공정을 개발하였다. 경계 요소법을 통해 추정된 일체화 성형 공정 시 금형 내부 온도는 정렬층 고유의 녹는점인 280°C 보다 낮은 250°C 부근에서 형성되었으며, 약 240~260 psi의 적층 압력 범위에서 성공적인 일체 성형 결과를 나타냄을 확인하였다. 또한 일체 성형된 전극은 고유의 CSCs(Charge Storage Capacity) 및 임피던스 값을 유지하였으며, 전극의 단선 및 합선 등의 물리적 손상을 억제하였음을 확인하였다.

약물 전달 성능 및 특성 분석은 크게 세 부분으로 진행하였다. 첫째, 사용한 Kevlar 섬유의 정·동적 모세관 유동 특성을 정량화하기 위해, 인가장력, 꼬임수 및 표면 상태에 따른 유체 이송 속도, 최대 이송거리 등에 대한 실험적 분석을 수행하였다. 둘째, 다공성 섬유와 생체 조직은 각기 고유한 흡수성을 지니고 있다. 전극 삽입 시, 이들 접합 계면에서 상이한 흡수율의 경쟁적 관계를 가정함으로써 섬유를 통해 주입된 약물의 조직 내 확산 특성을 분석하였다. 조직내 약물의 확산 특성이 인체 뇌조직과 유사한 1% agarose gel을 사용하였으며, 섬유의 모세관 유동 저항에 따라 조직내 약물 확산 범위 및 형태를 제어할 수 있음을 확인하였다. 끝으로, 약물 채널 시스템을 통한 약물 전달 능력 평가를 수행하였다. 가상 약물로서 Steroid 와 분자량이 유사한 Rhodamine (분자량 479 g/mol)과 대표적인 고분자 단백질인 FITC-BSA(분자량 66.4 kDa)를 사용하였다. 그 결과 본 약물 전달 채널을 통한 주입 유량은 약물의 농도, 대상 조직의 크기, 탑재된 섬유의 유동 저항에 따라 제어 가능함을 확인하였다.

가압 펌프와 직접 연결되어 약물을 이송하는 기존 연구 결과와 달리, 약물 저장/공급부와 섬유 기반의 약물 채널은 물리적 체결이 불가능하다. 따라서 통상적인 튜빙 방법에서 발전된 연결 방법(fitting joint)의 개발이 필수적이며, 본 시스템을 임상적으로 적용하기 위한 핵심 기술이다. 따라서, 소수성 격벽을 관통하는 섬유 가닥의 선택적 모세관 현상을 이용한 약물 저장/공급부 모듈을 개발하였다.

섬유 기반의 자력 이송 약물 전달 시스템은 별도의 가압 펌프가 필요하지 않기 때문에, 초소형 신경 보철 시스템 구성이 가능하다. 또한 주입 압력에 의한 대상 조직의 물리적 상해 위험성을 근본적으로 제거하였다. 한편, 섬유 기반 채널은 조직 내 삽입 시 발생할 수 있는 꺾임, 휘어짐 등 물리적 변형에 대해 높은 기계적 내구성을 지니며, 탑재된 섬유는 생체 조직에 의한 약물 채널 막힘 현상을 방지한다. 아울러, 채널을 구성하는 섬유의 유동 저항을 결정하는 기계적 특성을 조절함으로써 약물 전달 유량을 가변적으로 제어할 수 있기 때문에, 적용 대상의 약물 요구량에 따른 특성화된 약물 채널 시스템 제작이 가능하다. 향후, 섬유 재질, 필라멘트 수, 표면 처리 등 섬유의 유동 저항을 조절하기 위한 다양한 변수에 따른 약물 전달 특성 분석과 임상적 평가를 통해 섬유 기반의 자력 이송 약물 전달 시스템의 상용화 가능성을 한층 제고할 수 있을 것으로 기대한다.

핵심어: 자력 유체 이송, 모세관 현상, 약물 전달, 다공성 섬유, Kevlar, Liquid Crystal Polymer (LCP), 신경 보철(Neural Prosthesis), 장기 이식(Long-term Implantation)

학번: 2008-30857